Czech Technical University
Faculty of Nuclear Sciences and Physical Engineering
Department of Physics

Experimental study of the edge plasma of the Tore Supra tokamak

(Diploma thesis)

Martin Kubič

Supervisor:	Dr. James P. Gunn
Submitted:	14.5.2009

Prohlášení

Prohlašuji, že jsem svou diplomovou práci vypracoval samostatně a použil jsem pouze podklady uvedené v přiloženém seznamu.

Nemám závažný důvod proti užití tohoto školního díla ve smyslu § 60 Zákona č.121/2000 Sb., o právu autorském, o právech souvisejících s právem autorském a o změně některých zákonů (autorský zákon).

V Praze dne 14.5.2009 Martin Kubič

Acknowledgements

First of all, I would like to thank to my supervisor, Dr. James P. Gunn, for providing excellent guidance and practical support. Moreover, he gave me an access to all important scientific literature and necessary data. I am also especially grateful to M. Kocan and N. Fedorczak, both PhD students on Tore Supra in Cadarache, for help during my stay in Cadarache and for fruitful discussions.

Název práce:
Experimentální studium okrajhového plazmatu tokamaku Tore Supra.

Autor: Martin Kubič

Obor: Fyzikální inženýrství

Druh práce: Diplomová práce

Vedoucí práce: Dr. James P. Gunn, CEA Cadarache, Francie

Abstrakt: Studium okrajového plazmatu v tokamacích se v posledních letech prudce rozvíjí a je nyní jednou z hlavních součástí v oblasti výzkumu magnetické fúze. Sondové měření představují její nedílnou součást sprostředkující informace o toku plazmatu na stěny reaktoru. Výsledky prezetnované v tého práci pochází z experimentů na tokamaku Tore Supra zaměřených na ITER startup scénář. Principem tohoto scénáře je omezit výboj dvěmi diskrétními limitery na straně nízkého pole zatímco poloměr plazmatu se zvětšuje a hodnota bezpečnostního faktoru zůstává konstantní na hodnotě ~ 4.8. Vývoj analytického nástroje pro 3D analýzu magnetického pole a mapování magnetického pole společně s novou metodou pro určování polohy LCFS je také zmíněn.

Klíčová slova: Tore Supra, sondy, okrajové plazma

Title: **Experimental study of the edge plasma of the Tore Supra tokamak.**

Author: Martin Kubič

Branch of study: Physical engineering

Type of thesis: Diploma work

Abstract: The study of edge plasma physics in tokamaks has developed rapidly in recent years and is now considered as one of the major research areas of magnetic fusion. Edge probe techniques are a necessary experimental contribution to such studies, providing information about the plasma flux to the walls of the reactor. The experiments that were carried out on the Tore Supra tokamak to investigate the scrape-off layer conditions in ITER startup scenario are presented. The baseline of the ITER startup scenario is to limit the discharge on two discrete limiters on the low field side, increasing the minor radius while the safety factor is kept at a constant value ~ 4.8. Analytical tools for 3D magnetic connection analysis and magnetic field mapping together with a new method for LCFS evaluation are also presented.

Key words: Tore Supra, probes, edge plasma.

List of abbreviations

APL	...	Antenna Protection Limiter
CIEL	...	Internal Components and Limiter
CIMES	...	Components for Injection of Matter and Stationary Energy
HFS	...	High Field Side
ITER	...	International Experimental Thermonuclear Reactor
JET	...	Join European Torus
LCFS	...	Last Closed Flux Surface
LFS	...	Low Field Side
LHCD	...	Low Hybrid Current Drive
LP	...	Langmuir Probe
MHD	...	Magnetohydrodynamics
PF	...	Poloidal Field
RF	...	Radial Field
SOL	...	Scrape-Off Layer
TF	...	Toroidal Field
TP	...	Tunnel Probe
TPL	...	Toroidal Pumped Limiter
TS	...	Tore Supra

Contents

Chapter 1

Thermonuclear Fusion

1.1 Introduction

In astrophysics, fusion reactions power the stars and produce all but the lightest elements. Whereas the fusion of light elements in the stars releases energy, production of the heaviest elements absorbs energy, so that it can only take place in the extremely high-energy conditions of supernova explosions. In military applications, fusion of light elements provides the energy of thermonuclear explosions. If all goes well, we will manage to harness that fusion energy as a source of energy for mankind [1].

It takes considerable energy to force nuclei to fuse, even those of the lightest element, hydrogen. But the fusion of lighter nuclei, which creates a heavier nucleus and a free neutron, will generally release more energy than it took to force them together - an exothermic process that can produce self-sustaining reactions.

The energy released in most nuclear reactions is much larger than that for chemical reactions, because the binding energy that holds a nucleus together is far greater than the energy that holds electrons to a nucleus. For example, the ionization energy gained by adding an electron to a hydrogen nucleus is 13.6 eV - less than one-millionth of the 17 MeV released in the D-T (deuterium-tritium) reaction.

Any energy production from nuclear reactions is based on differences in the nuclear binding energy. Figure 1.1 shows the nuclear binding energy per nucleon (proton or neutron). It has been derived from measurements of the masses of the nuclei, when it was observed that the masses of nuclei are always smaller than the sum of the proton and neutron masses which constitute the nucleus. This mass difference corresponds to the nuclear binding energy according to Einstein's energy-mass relation $E = \Delta mc^2$.

From Figure 1.1 it is clear that there are two ways of gaining nuclear energy:

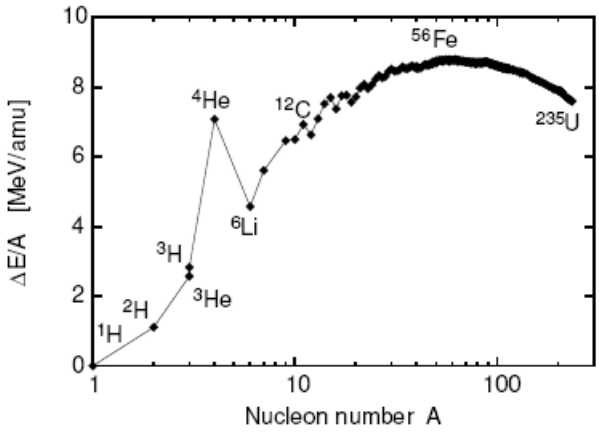

Figure 1.1: *Nuclear binding energy per nucleon as a function of the nucleon number A.*

1. By transforming heavy nuclei into medium-size nuclei: this is done by fission, e.g. of uranium.

2. By fusion of light nuclei into heavier ones: in particular the fusion of hydrogen isotopes into stable helium offers the highest energy release per mass unit. Doing this in a controlled manner has been the goal of fusion research for about 40 years.

The energy release per nucleon is of the order of 1 MeV ($= 10^6$ eV) for fission reactions and in the order of a few MeV for fusion reactions. This is 6-7 orders of magnitude above typical energy releases in chemical reactions, which explains the effectiveness and potential hazard of nuclear power.

1.2 Fusion on the sun

Nuclear fusion of light elements is the source of energy produced in the stars including our sun which maintains life on our planet. In the stars, the condition necessary for fusion as regards temperature, density, and confinement time are maintained by gravity. On the sun the main reactions are the following:

$$\begin{aligned} p + p &\longrightarrow D + e^+ + \nu_e \\ D + p &\longrightarrow {}^3He + \gamma \\ {}^3He + {}^3He &\longrightarrow {}^4He + 2p \end{aligned}$$

where p denotes a proton, D a deuteron, a heavy hydrogen isotope with one proton and one neutron, ^{3}He, ^{4}He are helium isotopes, γ stands for a high-energy photon, e^+ for a positron and ν_e for an electron neutrino [1].

Further reactions which are important at temperatures above about 1 keV, produce ${}^{7}_{4}\mathrm{Be}$, ${}^{7}_{3}\mathrm{Li}$, ${}^{8}_{5}\mathrm{B}$ and ${}^{8}_{4}\mathrm{Be}$, which decays into $2\,{}^{4}_{2}\mathrm{He}$ nuclei. Also in these reactions neutrinos are produced, however with a higher kinetic energy than those from the pp-reactions mentioned above.

1.3 Fusion on earth

Possible candidates for using fusion energy on earth are the following reactions (T denoting tritium, the heaviest hydrogen isotope with 2 neutrons):

$$\begin{aligned}
D + D &\longrightarrow {}^{3}He + n + 3.27MeV \quad (50\%)\\
D + D &\longrightarrow T + p + 4.03MeV \quad (50\%)\\
D + {}^{3}He &\longrightarrow {}^{4}He + p + 18.35MeV\\
D + T &\longrightarrow {}^{4}He + n + 17.59MeV\\
p + {}^{11}B &\longrightarrow 3\cdot {}^{4}He + 8.7MeV
\end{aligned}$$

The first four reactions (for which the cross sections are shown in Figure 1.2) can be summarized as

$$3D \longrightarrow {}^{4}He + p + n \quad 21.6MeV$$

and therefore rely on deuterium as fuel only. All the reaction cross sections in Figure 1.2 show a steep increase with the relative energy, but the D-T reaction

$$D + T \longrightarrow {}^{4}He + n + 17.59MeV$$

has by far the largest cross-section at the lowest energies. This makes the D-T fusion process the most promising candidate for an energy-producing system. To be a candidate for an energy producing system, the fusion fuel has to be sufficiently abundant. Deuterium occurs with a weight fraction of $3.3\cdot 10^{-5}$ in water. Given the water of the oceans, the static energy range is larger than the time the sun will continue to burn.

Tritium is an unstable radioactive isotope. It decays to

$$T \longrightarrow {}^{3}He + e^{-} + \bar{\nu}_e$$

with a half-life of 12.3 years. Tritium can be produced with nuclear reactions of the neutrons from the D-T reaction and lithium:

$$\begin{aligned}
n + {}^{6}Li &\longrightarrow {}^{4}He + T \quad +4.8MeV\\
n + {}^{7}Li &\longrightarrow {}^{4}He + T + n \quad -2.5MeV
\end{aligned}$$

The ultimate fusion fuel will thus be deuterium and lithium. The latter is also very abundant and widespread in the earth's crust and even ocean water contains an average concentration of about 0.15 ppm of lithium.

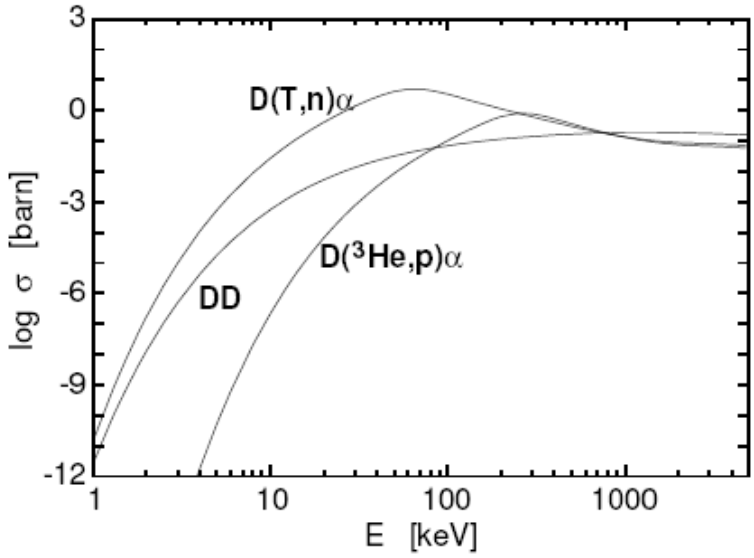

Figure 1.2: *Measured cross-sections for different fusion reactions as a function of the center of mass energy.*

1.4 Ignition

To initiate nuclear fusion it is necessary to put together nuclei of specific light atoms close enough to overcome the strong repulsive electrostatic forces and allow the nuclear force to act. Because of quantum mechanical tunneling, D-T reaction occurs at energies somewhat less than that required to overcome the Coulomb barrier. As a D-T plasma is heated by external power sources to thermonuclear conditions the α-particle heating provides an increasing fraction of the total heating power. When adequate confinement conditions are provided, a point is reached where the plasma temperature may be maintained against the energy losses solely by α-particle heating. The applied external heating then can be switched off and the plasma temperature is sustained by internal heating only [2]. The requirement for the plasma burn to be self-sustaining can be written as

$$n\tau_E > \frac{12}{\langle\sigma v\rangle}\frac{T}{E_\alpha} \tag{1.1}$$

where τ_E is energy confinement time, which is a ratio of total energy of plasma and total power loss, respectively, $\langle\sigma v\rangle$ is reaction rate and E_α is energy of α-particle. The right-hand side of inequality (1.1) is a function of temperature only and it has minimum close to $T = 30keV$. However, since τ_E is itself a function of temperature, the temperature at the minimum is not to be taken as an optimum condition. Moreover, from reactor point of view, the optimum temperature is not as high as that corresponding to the energy of maximum cross-section because the required reactions occur in the high energy tail of the Maxwellian distribution of heated particles.

The condition for ignition can be expressed in so called Lawson criterion [3] (or triple product) which gives for the D-T reaction:

$$nT\tau_e > 3.10^{20} m^{-3} keVs \tag{1.2}$$

This is a very convenient form for the ignition condition since it brings out clearly the requirements on density, temperature and confinement time. The precise value of the constant in condition (1.2) depends on the profiles of n and T. The condition (1.2) is valid for flat profiles.
A measure of the success in approaching reactor conditions is given by the power amplification factor Q, a ratio of the thermonuclear power P_f produced to the heating power P_H supplied, that is:

$$Q = \frac{P_f}{P_H} \tag{1.3}$$

There are two ways how to reach ignition:

1. To maximize confinement time: the hot plasma is confined by strong magnetic fields leading to maximum densities of about $1.5 \cdot 10^{20} m^{-3}$, which is $2 \cdot 10^5$ times smaller than the atom density of a gas under normal conditions. With these densities, the energy confinement time required is in the range of 2 to 4 seconds. This approach is the main line in fusion research today and it is called *'magnetic confinement fusion'*

2. The other extreme is to maximize the density. This can be done by strong, symmetric heating of a small D-T pellet. The heating can be done with lasers or particle beams and leads to ablation of some material causing implosion due to momentum conservation. It is clear that the energy confinement time is extremely short in this concept: it is the time required for the particles to leave the hot implosion center. The density required is about 1000 times the density of liquid D-T. Since it is the mass inertia which causes the finiteness of this time, this approach to fusion is often called *'inertial fusion'*.

1.5 Magnetic confinement fusion

For last 50 years, the scientists in fusion research aim to develop an electricity producing power plant based on the fusion reaction between the nuclei of the hydrogen isotopes: deuterium and tritium. The principal concept, to achieve the thermonuclear fusion on Earth is to confine a plasma consisting of light atomic nuclei and their electrons in a magnetic field configuration in such a way that the thermal plasma can reach conditions necessary to achieve a positive energy balance [4]. The Lorentz force makes charged particles move in helical orbits (Larmor orbits) about magnetic field lines. In a uniform

magnetic field and in the absence of collisions or turbulence, the particles (better their guiding centers) remain tied to the field lines, but are free to move along them. The distance between the actual particle orbit and the magnetic field line is the Larmor radius r_L. A magnetic field is thus capable of restricting the particle motion perpendicular to the magnetic field but does not prevent particles from moving along the magnetic field. This effect serves as the basis for all magnetic confinement schemes. To avoid losses from the edges, it is necessary to close both edges together by creating a torus (Figure 1.3) [5]. For one single particle in a toroidal device, the confinement is perfect. Unfortunately, in reality, particle collisions, drifts and MHD turbulence lead to a transport of particles and energy.

The products of the D-T fusion reactions are helium nuclei (α-particles) and neutrons. The first, also bound to the magnetic field lines, are supposed to transfer their energy to the thermal plasma and thus sustain the fusion reaction. The latter, because they are not confined by the magnetic field, can leave the plasma directly and will be used to breed tritium from lithium and convert the fusion energy into heat. Through the last few decades was invented many magnetic configurations for applications to nuclear fusion. Nowadays, the most viable concepts today are the tokamak and the stellarator invented in 1950s.

1.5.1 Tokamak

A tokamak is a toroidal device in which the poloidal magnetic field is created by a toroidal current I_p flowing through the plasma. Figure 1.3 gives a schematic view of a tokamak. A strong toroidal magnetic field is generated by a TF coil system. The toroidal current is induced by the transformer effect. The plasma itself serves as a secondary winding of the transformer, while the primary is wound on central core. The toroidal geometry of the plasma leads to two hoop forces, which are both in the direction to expand the plasma ring. The first of these forces results from the natural tendency of a current loop to expand in an effort to lower its magnetic energy. The second force is the resultant of the sum of centrifugal and grad-B forces experienced by the individual particles during their motion along the field lines [5, 2]. Providing a vertical magnetic field that interacts with the toroidal current to give an inward force can compensate both these forces. If the applied vertical field is spatially non-uniform and increases with major radius, the plasma is found to be vertically unstable. In an attempt to increase the plasma pressure, the plasma is pushed as much as possible to the high field side, thus creating a D-shaped plasma, i.e. having elongation and triangularity. An externally applied horizontal magnetic field B_h can then be used to maintain the plasma well centered. Both the horizontal and vertical position control is in all modern tokamaks achieved by means of feedback

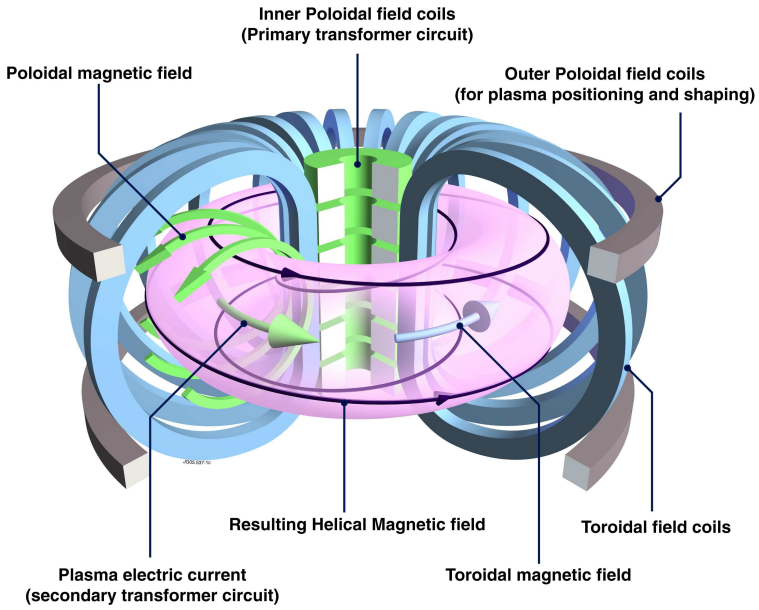

Figure 1.3: *Schematic view of a tokamak.*

controlled vertical and horizontal magnetic field systems. The combination of the above fields can generate an equilibrium tokamak configuration. Whether this equilibrium will be stable or unstable can be found from a stability analysis.

There exists another magnetic configuration, called a stellarator, in which the magnetic field is provided completely by external toroidal as well as poloidal coils. The fact of not having an intense current flowing in the plasma is an advantage in the event of plasma disruption, but the drawback is the complexity of the necessary magnetic coils. This may be seen on the Figure 1.4 of the German stellarator project W7X [6], where the coils are represented in blue and the plasma in orange colour [7].

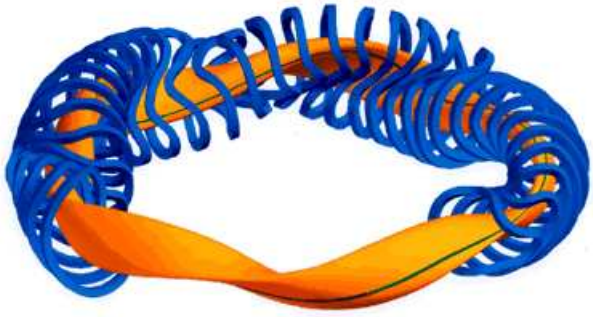

Figure 1.4: *Schematic view of a stellarator.*

1.5.2 Tore Supra

Tore Supra is a large tokamak with major radius R = 2.42 m and minor radius a = 0.72 m with superconducting TF coils, which are able to produce a magnetic field up to 4.5 T. It total, there are 18 superconducting TF coils which are cooled by superfluid He at temperature of about 1.8 K. Tore Supra is the only tokamak fully equipped with actively cooled plasma facing components [1]. The cooling is provided by a high pressure water loop with a temperature of about 200 °C, flow speed of 10 $m \cdot s^{-1}$, and pressure of 40 bars. This allows, together with the LHCD current drive and heating system, high performance and long duration discharges [8].

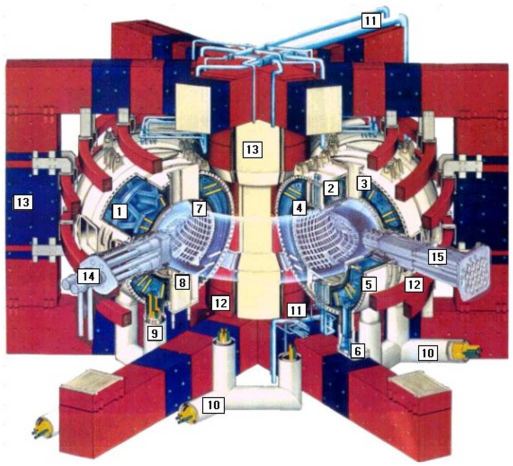

Figure 1.5: *Schematic view of the Tore Supra tokamak.*

Plasma major radius	2.42 m
Plasma minor radius	0.72 m
Pulse length (inductive only)	30 s
Toroidal magnetic field	< 4.5 T
Plasma current	< 1.7M A
Volt-seconds to drive plasma current	15 Vs
Total additional heating power	14 MW

Table 1.1: *Main Tore Supra parameters*

The first plasma was attained in Tore Supra in April 1988. Since that time the supercon-

[1] 98% of all surfaces in direct view of the plasma have water flowing in them, even the internal walls of the tall vertical ports.

ducting magnet worked with no major failures. This represents a significant technological success and an important progress for the feasibility of the programme of controlled thermonuclear fusion. In 1996 a record was reached with a plasma duration of two minutes with an induced current of almost 1 MA generated non inductively by 2.3 MW of lower hybrid frequency waves (i.e. 280 Mjoules of injected and extracted energy). This result was possible due to the actively cooled plasma facing components installed in the machine from the beginning. This result opened the way to the active control of steady state plasma discharges and the associated physics. The search for enhancement of performances has triggered new technological developments for plasma facing components (CIEL project) and non inductive current drive by electromagnetic waves (CIMES project). The new CIEL configuration was implemented in 2001 and the CIMES project is being progressively implemented. Thanks to the new CIEL configuration, a new world record was reached in 2003. A plasma discharge of 6.5 minutes was achieved with over 1000 MJ of energy injected. The first step of improvement is the new LH antenna (plus steady state klystrons), which is being installed now. First test of new LH antenna are planned in November 2009.

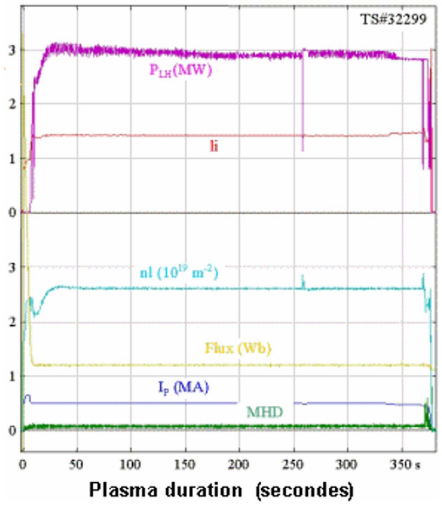

Figure 1.6: *The main plasma parameters profiles of the longest discharge ever reached on Tore Supra.*

The purpose of Tore Supra is to obtain long stationary discharges, thus addressing two major questions: non-inductive current generation and continuous heat and particles removal. The physics programme therefore has two principal research orientations, complemented by studies on magnethydrodynamic (MHD) stability, turbulence, and transport. The first physics programme concerns the interaction of electromagnetic (Lower Hybrid and Ion Cyclotron) waves with the hot central plasma. All or part of the plasma current

can be generated in this manner, thus controlling the current density profile. This is an important contribution to the concept of an "advanced tokamak". In 1996 notable progress was made, allowing totally non-inductive shots over a period of 75 s to be obtained. The second physics programme concerns the edge plasma and its interaction with the first wall.

On Figure 1.7 are shown temporal evolution of basic parameters of a typical ITER startup scenario discharge on Tore Supra in which the plasma is limited on discrete limiter on the low field side. ITER startup scenario will be described in detail in section 5.1 It is not the main goal now to produce long discharges on Tore Supra. Standard TS discharge is $\sim$ 20 - 30 s long which is enough to perform all necessary plasma studies. Discharge

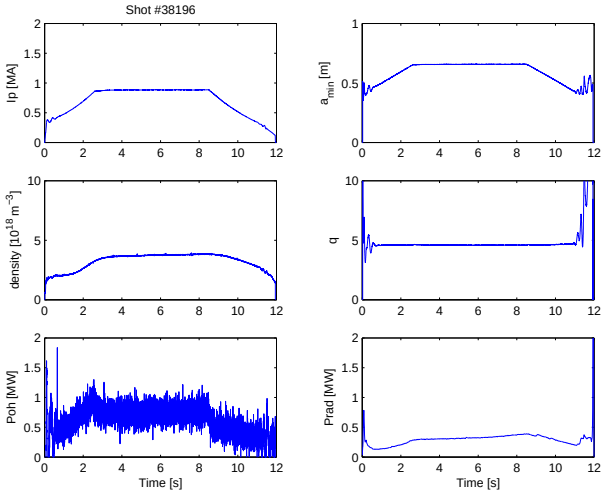

Figure 1.7: *Typical Tore Supra discharge parameters profiles for the ITER startup scenario.*

breakdown is made in a puff of the working gas, deuterium. The plasma current (top left panel) is controlled by real time feedback on the safetey factor (middle right panel), which is programmed to a constant value q = 4.8. The minor radius is ramped up in the first 2 s of the discharge (top right panel). Density (middle left panel), ohmic power (lower left panel), and radiated power (lower right panel) remain relatively constant.

Chapter 2

Edge Plasma Physics

2.1 Introduction

A major issue in the design and construction of a nuclear fusion reactor with a magnetically confined plasma is the interaction of the hot plasma with the material components of such a device. On the one hand, the plasma facing vessel components represent a sink for energy and particles released by the plasma. On the other hand, the particle bombardment of the material surface may lead to release of wall atoms and of previously implanted fuel atoms which in turn may enter the plasma.
The contamination of the plasma by impurities released from the vessel structure is one of the main problems caused by plasma wall interaction processes. An additional problem is the alteration of the material structure by the particle bombardment and the high energy flux which may limit the lifetime of the plasma facing components significantly. These problems must be solved under the constraint that the generated power has to pass through the vessel components at some location. The wall may further act as a reservoir for the hydrogen fuel isotopes leading to an uncontrollable additional source of fuel atoms, which may cause problems in maintaining stationary discharge conditions [1]. Moreover, the retention of tritium in the wall must be limited to comply to radiation and safety constraints. In the following will be introduced plasma facing components and a basic model of the edge plasma region in contact with the walls, the so-called scrape-off layer (SOL).

2.2 Plasma facing components

In a fusion reactor, we can find several components facing the plasma directly. The largest surface consists of the first wall which surrounds the bulk region of the plasma

torus. The plasma shape may be restricted by additional limiters to protect the vessel wall or equipment like antennas for radio-frequency heating or optics of some diagnostic systems which cannot withstand excessive heat loads. Finally, a very important part of the plasma facing components in current and future fusion devices are the divertor target plates. In a diverted plasma configuration these plates provide the main plasma-surface interaction zone. The fraction of the fusion power carried by the produced α-particles is coupled out to a large extent through these areas.

Magnetic field lines which lie on a flux surface that never makes contact with a solid surface are called closed, while those which pass through a solid surface are termed open. The border of the confined region is known as the Last Closed Flux Surface (LCFS) or separatrix, while the term Scrape-Off Layer (SOL) designates a narrow region (usually only a few cm wide) outside this border. The SOL may be imagined as the region where the plasma is essentially scraped off from the core plasma (Fig. 2.1). Particles are moving not only along field lines but can move perpendicular to magnetic field lines mainly due to turbulent transport and drifts. The width of the SOL can be then defined as the mean radial distance that particle moves during parallel time of flight along one connection length.

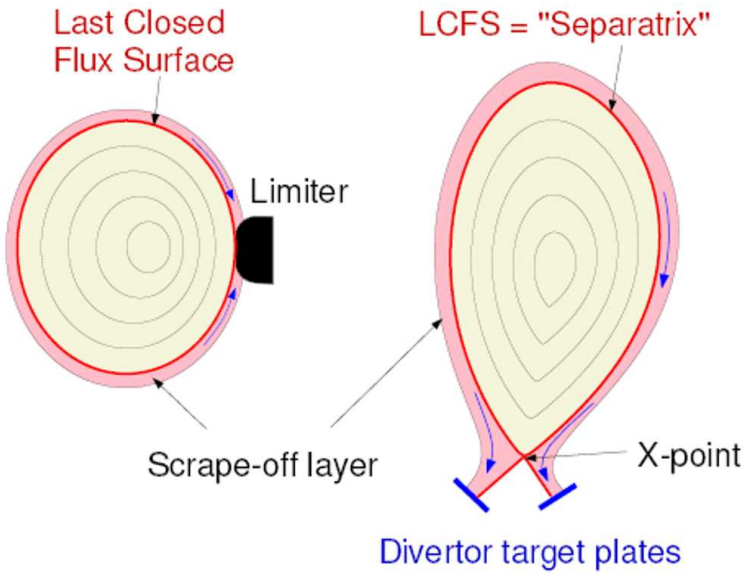

Figure 2.1: *Limiter and divertor configurations.*

There are two ways by which the last closed field line can be delimited, see Fig. 2.2. In the simplest and historically earlier option the confined region is "limited" by inserting a barrier a few cm into the plasma. This is called a limiter and essentially it was there to protect the walls from the hot core plasma. Large impurity fluxes from sputtered limiter material prevented the achievement of hot, clean plasmas.

Therefore a more sophisticated solution was developed about 20 years ago, using a modification of the magnetic field lines at the plasma edge, so that the field lines of the SOL are diverted into a dedicated region where the plasma exhaust ends up in collisions with the wall (the target plates) or with gas. This configuration, called a divertor, has proved in experiments to be significantly more advantageous because it reduced significantly the direct "line-of-sight" contamination of the core plasma by sputtered impurity atoms [9].

2.2.1 Limiter

A limiter is a solid surface which defines the edge of the plasma. Limiters take various geometrical forms as illustrated in Fig. 2.2. The simplest concept is a circular hole in a diaphragm normal to the toroidal field. This is known as a poloidal limiter. Because magnetic field lines in a tokamak form closed surfaces, even a local or point interaction will in principle define a boundary. In either case there will be a decreasing plasma density radially outside the limiting surface, due to parallel losses in the scrape-off layer. In the case of a complete poloidal limiter the connection length L will be approximately the circumference of the torus, $2\pi R$. In the case of the toroidal limiter the connection length L is longer, as the particles need to go around the chamber several times before hitting the solid surface. The connection length depends on the pitch angle via the safety factor q and it can be expressed as $\sim 2\pi Rq$. The plasma scrape-off layer will thus be broader.

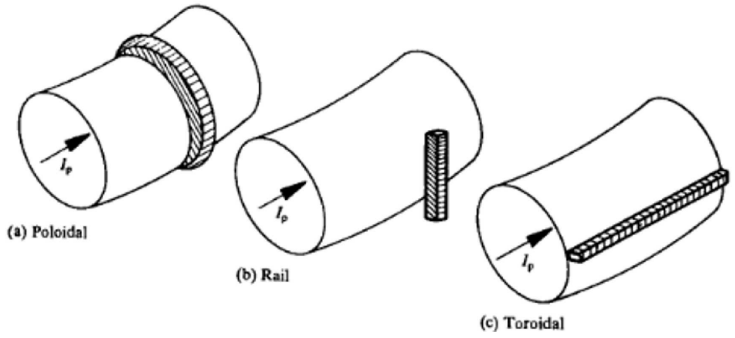

Figure 2.2: *Schematic representation of different types of limiter.*

A limiter plays a number of roles in tokamak operation. It serves mainly as a wall protection from the plasma (disruption, runaway electrons or other instabilities). For this reason it is commonly made of a refractory material, such as carbon, molybdenum or tungsten, capable of withstanding high heat loads. Secondly, the limiter localizes the plasma-surface interaction. The high power and particle' density at the limiters surface causes rapid removal of absorbed gas, oxide layers and other desorbed impurities. Finally, the limiter localized the particle recycling. A higher neutral density and more radiation

is observed in the region near the limiter than at other positions around the torus [2].

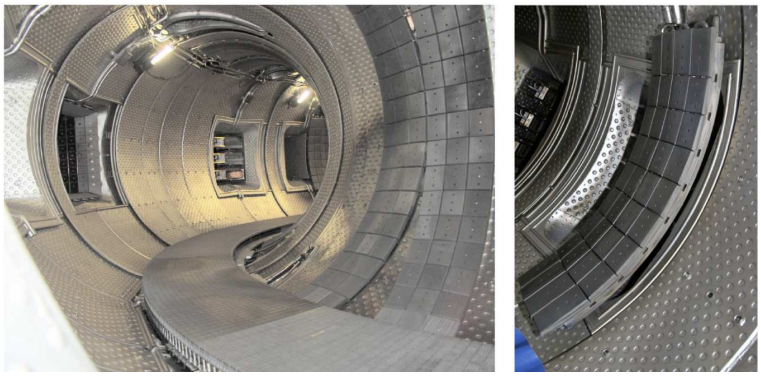

Figure 2.3: *Toroidal pumped limiter of the Tore Supra tokamak placed at the bottom of the chamber (left) and modular limiter placed at the midplane (right).*

2.2.2 Divertor

In the case of a limiter the last closed flux surface is defined by a solid surface and consequently neutral impurity atoms released from the surface can enter the confined plasma directly. In a divertor the LCFS is defined solely by the magnetic field and plasma surface interactions are remote from the confined plasma. In the divertor configuration impurities released from the target are ionized and may be swept back to the target by the plasma flow before they can reach the LCFS and enter the confined plasma.

There are several possible magnetic configurations for a divertor, but the most exploited until now is the toroidally symmetric or poloidal field divertor which corresponds to the toroidal limiter [2, 10]. The required magnetic field is produced by toroidal conductors which create a null (X-point) in the poloidal field and a separation of open and closed magnetic surfaces. These divertors have the advantage of preserving the essential axisymmetry of the tokamak and can be combined with D-shaped or elliptical cross-sections. It has been found experimentally that use of this divertor configuration often results in a significant improvement in the energy confinement time and to discovery of the H-mode [11].

A construction of a divertor is more difficult than the construction of a limiter since it requires external PF coils conducting high current (comparable with the plasma current). This configuration is used in the European facilities such as JET, COMPASS, ASDEX, TCV and MAST, and it is designed also for the tokamak ITER. For large devices with high energy stored in plasma, the geometry of divertor tiles must be designed in a special way, in order to maximize surface touched by plasma and thus to minimize the energy flux to divertor plates.

2.3 The scrape-off layer

As shown in Fig. 2.2 the plasma edge in a magnetically confined plasma is either defined by a material limiter or, in the case of a diverted plasma, by a magnetic separatrix. Inside the so defined boundary, the magnetic surfaces are closed while in the region between the boundary and the wall surface, the so called scrape-off layer, the field lines intersect material components. The particle exhaust and the α-particle fraction of the produced power (as well as the additional heating power during start-up) are coupled out to a large extent through this region and transferred to the limiters or divertor plates.

2.3.1 Simple SOL model

With simple estimates we may now characterize some basic features of the scrape-off layer such as the SOL thickness and the radial density variation, assuming a simple SOL with perpendicular diffusion as particle source for the SOL (see Fig. 2.4). The basic feature of the simple SOL is that the distance between the LCFS and the first wall is sufficiently large that the plasma density decays naturally to zero. In the other words, all charged particles hit the main limiter or divertor plates; none hit the first wall. However, for reasons of economy, plasmas are shaped so as to occupy as much of the vacuum chamber volume as possible. In addition all tokamaks have secondary limiters (poloidal limiters, antenna protection limiters, etc). Hence a significant interaction with the SOL plasma can occur. The simple SOL structure is disturbed leading to formation of "complex" SOL (see section 5.5) which requires a 3D analysis.

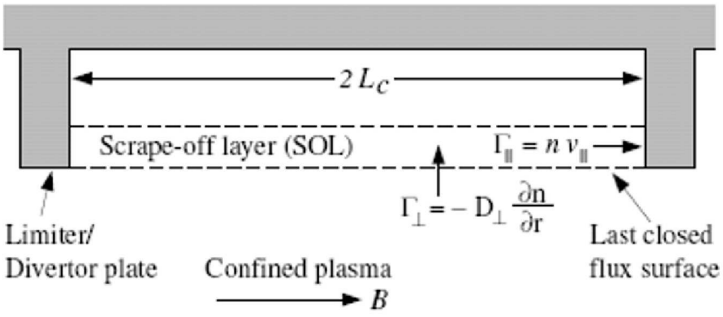

Figure 2.4: *The simple SOL model*

For this first estimate we may relate the length of the flux tube L and the SOL thickness to the average transport velocities $v_\parallel$ and $v_\perp$ to

$$\frac{v_\perp}{v_\parallel} = \frac{\lambda}{L} \tag{2.1}$$

Let us take for the average velocities $v_\parallel = 0.5c_s$ and $v_\perp n = D_\perp \partial n/\partial x$. With the characteristic length $\lambda = (1/n)\partial n/\partial x$ we obtain

$$\frac{D_\perp/\lambda}{0.5c_s} = \frac{\lambda}{L} \tag{2.2}$$

By separating λ we get the well known expression for the SOL thickness λ (i.e. the density decay length) [1]

$$\lambda = \sqrt{\frac{D_\perp L}{0.5c_s}} \tag{2.3}$$

With typical values for an edge plasma $D_\perp = 1m^2/s, T = 50eV$, and $L = 10m$ we obtain $\lambda = 30mm$. Despite of fact that $D_\perp$ is an empirical results based on SOL measurements of λ, L, and c_s, there is no first-principle derivation of it. It is believed the "effective" D that gives rise to the observed decay lengths is due to turbulent transport.

This is a remarkably small value compared to the dimensions of a fusion reactor. As a consequence, the surface area wetted by the plasma reduces by roughly two orders of magnitude with respect to the total wall area, leading to unacceptable high heat loads. The radial variation of density inside the SOL can be derived from a simple 1D-calculation based on the conservation of mass along the flow channel z

$$\frac{\partial}{\partial x} D_\perp \frac{\partial n}{\partial x} = \frac{\partial}{\partial z}(n v_\parallel) \tag{2.4}$$

Assuming in a first step $D_\perp = \text{const.}$ and $\partial n/\partial x = \text{const.}$ along z as well as a constant right hand site of Eq. (2.4) represented by $\partial/\partial z(n v_\parallel) = n/\tau_\parallel$ with a characteristic particle residence time in the SOL given by $\tau_\parallel = L_\parallel/c_s$ (parallel transport to the target is the only plasma sink, no particle sources caused by ionization of neutrals inside the SOL are considered) we obtain the solution of Eq. (2.4)

$$n(x) = n(0) exp(-x/\sqrt{D_\perp \tau_\parallel}) \tag{2.5}$$

The problem is that in reality both $L_\parallel$ and c_s can vary radially. The density shows an exponential decay inside the SOL with a characteristic length $\lambda = D_\perp \tau_\parallel$ as given by Eq. (2.3), $n(0)$ denotes the density at the LCFS. Here, the typical time scale of parallel transport to the targets τ is of the order of ms. However, one has to be careful when using these simple expressions, as particle sources inside the SOL and drifts will alter the result [12, 13]. Moreover, these simple 1D estimations provide only a basis for general idea about SOL, but cannot be used for real machines which require in all but the most simple cases full 2D or even 3D models

[1] This expression can be found in much literature also in the form $\lambda = \sqrt{\frac{D_\perp L}{c_s}}$ [12]. Only radial particle transport is consider here. In reality, the diffusion exist also in toroidal and poloidal direction.

2.3.2 General description of parallel transport in the SOL

He we outline some of the basic features of the isothermal fluid model of 1D flow along the SOL [12]. These results are discussed in detail either in the subsequent sections or in the reference [14]

1. The plasma fluid flow along the SOL due to the parallel pressure gradient which is induced in the SOL plasma by the presence of particle source and sink. The total pressure is constant along B, but the static pressure decreases, providing the force: $p_{total} = p_{static} + p_{dynamic}$, where $p_{dynamic} = mnv^2$; thus as p_{static} drops, the flux of flow momentum, mnv^2, increases, and v increases [15]. See Fig. 2.5.

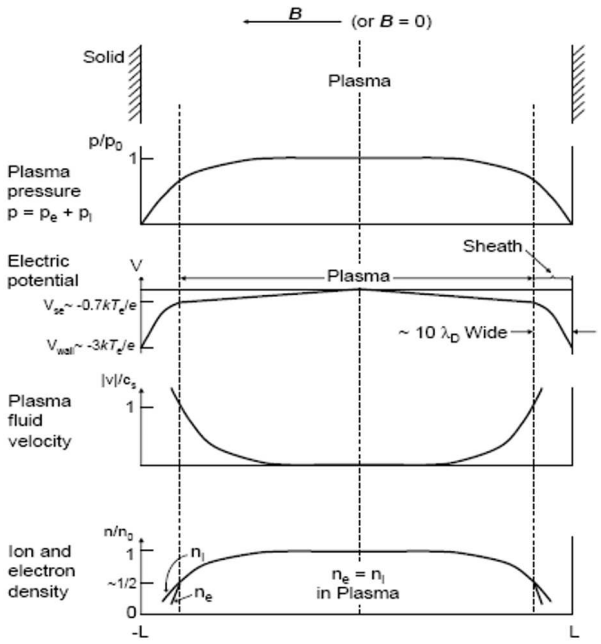

Figure 2.5: *Schematic of the variation of the plasma pressure, electric potential, plasma velocity and ion/electron densities in the plasma between two semi-infinite planes. The thickness of the sheath is exaggerated for clarity. The total length is 2L.*

2. In the first few μs after the plasma is initiated, i.e. just after ionization of the gas in the vacuum vessel, the electrons, due to their small mass and high mobility, rush ahead of the ions and strike the solid surface, charging them up negatively.

3. Consequently, the loss rate of the ions and electrons becomes equal – defined as ambipolar plasma transport – i.e. an ambipolar electric field arises in the plasma. The solid surface will spontaneously charge up to a potential of wall $V_{wall} \sim -3kT_e/e$, for hydrogenic plasma, relative to the plasma potential.

4. Electrostatic potentials on the surface containing plasma are almost entirely shielded out within a very short distance of the order of the Debye length [16, 17],

$$\lambda_{Debye} \;=\; \left(\frac{\epsilon_0 k T_e}{n_e e^2}\right)^{1/2} \tag{2.6}$$

5. The shield is not perfect, however, and a small electric field $E = kT_e/2eL$, penetrates throughout the length of the plasma where the particle source exists. This is called the pre-sheath electric field, corresponding to the pre-sheath potential drop of $V_{se} \sim -0.7kT_e/e$, and it acts on the ions in the SOL to help move them toward the target.

6. The surface sink action causes a depression of the local plasma density creating a parallel density and pressure gradient. The pre-sheath field acts to retard the electrons, which come into a nearly perfect parallel momentum, balance between a parallel pressure gradient force pushing the electrons toward the surface and the retarding electric field force. The electrons thus obey, almost perfectly, a Boltzmann relation [18]

$$n \;=\; n_0\, exp[eV/kT_e] \tag{2.7}$$

   where n_0 is the plasma density upstream where the plasma potential is taken to be V = 0.

7. It will be shown that both charged species have a fluid speed which reaches the ion acoustic speed: $c_s = [k(T_e + T_i)/m_i]^{1/2}$ just as the particle enters the sheath that is $v_{se} = c_s$, where v_{se} is the velocity at the sheath edge.

8. The plasma density drops from n_0 at the distance L upstream to $n_{se} = \frac{1}{2}n_0$ at the sheath edge.

2.3.3 The Sheath

The space within the vessel occupied by the charged particles consists of two regions:

- the plasma which usually fills the vast majority of the available space. The plasma is by definition the region where $n_e \cong \sum_i n_i Z_i$, i.e. the plasma is electrically quasineutral, or at least $n_e \approx n_i$, i.e. quasineutrality holds.

- The sheath, i.e. the region of net charge, usually in a thin region adjacent to a solid surface and $n_e < \sum_i n_i Z_i$ in the sheath. The thickness of the sheath is several Debye lengths (a typical value for most tokamaks is around 0.1 mm).

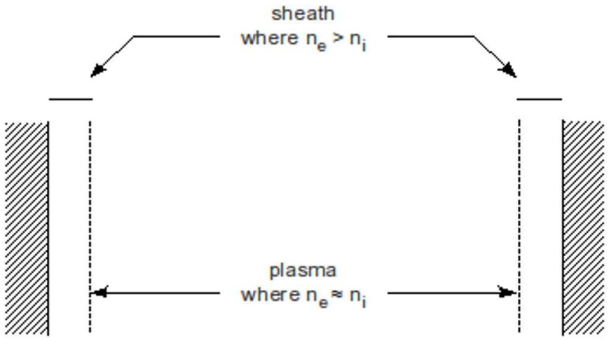

Figure 2.6: *The space available to charged particles is divided into the quasineutral plasma and pre-sheath, which is characterized by net space-charge density.*

2.3.4 Simple derivation of the Bohm criterion for $T_i = 0$

Consider the sheath where $n_e \neq n_i$. For the electron density we assume that the Boltzmann relation (Eq. 2.7) holds, since the electrons find themselves in a repulsive, i.e. confining, electric field and suffer such loss that 'v_e^{loss}' ($\equiv v_{se}$) $\ll \bar{c}_e$. As a result, the electron velocity distribution is approximately Maxwellian, even in the sheath, T_e remains constant, and the electron density in the sheath, where the local potential is $V(x)$, simply falls off according to a Bolzmann factor:

$$n_e(x) \; = \; n_{se}\, exp[e(V \; - \; V_{se})/kT_e] \tag{2.8}$$

where $n_{se,e} = n_{se,i} = n_{se}$ is the density at the sheath entrance. This potential distribution constitutes a hill for the electrons ($V < 0$), as the limiter or divertor surface has initially been charged negatively by the electrons. Here we are taking the reference potential to be $V = 0$ at a location in the plasma some distance upstream from the sheath edge. V_{se} describes the potential drop which occurs upstream of the sheath edge (in the plasma itself), i.e. the pre-sheath electric field. We want to know how strong this pre-sheath potential drop is: for the case of $T_i = 0$ together with the assumption that all the ions originated at a single location upstream of the sheath edge – this is the same thing as finding the the 'plasma exit velocity' v_{se}, since with these assumptions

$$\frac{1}{2} m_i v_{se}^2 \; = \; -e\Delta V_{pre-sheath} \; = \; -eV_{se} \tag{2.9}$$

In addition, it is assumed that the ions falls collisionlessly through a pre-sheath potential drop V_{se}.

The ions will be accelerated in the sheath. If we assume now following that the parallel ion flux density remains constant within the very thin sheath, $n_i v_i = const.$, and for a moment that $T_i = 0$, we can use ion energy conservation $\frac{1}{2} m_i v_i \; = \; -eV$ (no change of thermal energy) to obtain

$$n_i \; = \; n_{se}(V_{se}/V)^{1/2} \tag{2.10}$$

Within the plasma we assume $n_e = n_i$, but in the sheath $n_e < n_i$ and we need an equation to relate n_e, n_i and V. This is given by the Maxwell equation $div\,\mathbf{E} = e(n_i - n_e)/\epsilon_0$, which, with the $\mathbf{E} \equiv -\nabla V$, gives us the 1D Poisson's equation:

$$\frac{d^2V}{dx^2} = -\frac{e}{\epsilon_0}(n_i - n_e) \tag{2.11}$$

and thus

$$\frac{d^2V}{dx^2} = -\frac{e}{\epsilon_0} n_{se} \left[\left(\frac{V_{se}}{V} \right)^{1/2} - exp[e(V - V_{se})/kT_e] \right] \tag{2.12}$$

Now, if we use consider a small region inside the sheath where $\Delta V \equiv V_{se} - V > 0$ and use Taylor expansion together with differential equation theory, we finally obtain

$$v_{se} \geq c_s \tag{2.13}$$

which defines the *Bohm criterion* [19] for the 'plasma exit velocity'. [2]

It has to be noted that the above derivation of the Bohm criterion is for very simple case concerning the following assumptions:
(a) particle source is a delta function in space,
(b) the ions are monoenergetic, Ti = 0,
(c) there are no collisions.
Relaxation of assumptions (a) and (b) to more realistic ones results in only modest changes to c_s and V_{se}, as in next section. Ion-ion collisions are not of much importance, but if the ions suffer momentum-loss collisions to neutrals, then $|V_{se}|$ can become very large [12].

2.3.5 The Bohm criterion when $T_i \neq 0$

Allowing for $T_i \neq 0$ rather complicates the analysis, but it is nevertheless carried out the same way as in the previous section. The final result turns out to be expressible in a rather compact way, the generalized Bohm criterion [20]:

$$\int_0^\infty \frac{f'_{se}(v)dv}{v^2} \leq \frac{m_i}{kT_e} \tag{2.14}$$

where $f'_{se}(v)$ is the 1D ion velocity distribution at the sheath edge.

Next, consider the situation where $T_i \neq 0$ and let us take $f'_{se}(v)$ to be normalized shape

$$f'_{se}(v) = \begin{cases} (2c_i)^{-1}, & \text{for } v_{se} - c_i \leq v \leq v_{se} + c_i \\ 0, & \text{otherwise} \end{cases} \tag{2.15}$$

[2] A strong assumption is used here: an oscillatory sheath potential, $V(x)$ is supposed. Anyway, oscillatory sheath potential has never been experimentally observed! In addition, a monotonic sheath potential has never been seen either as well as Bohm criterion has never been successfully confirmed.

where we define $c_i \equiv (kT_i/m_i)^{1/2}$, essentially the ion thermal speed. Insertion of this distribution into equation (2.15) gives the anticipated result:

$$v_{se} \geq c_s = [(kT_e + kT_i)/m_i]. \tag{2.16}$$

2.3.6 The particle flux density to a surface

Using this Bohm criterion we can describe the ion flux density to the target as the parallel flux density at the sheath entrance (se) (neglecting additional sources in the very thin sheath)

$$\Gamma^i_{target} = n_{se}c_s = \frac{1}{2}n(0)\sqrt{\frac{k(T_i + T_e}{m_i}} \tag{2.17}$$

To preserve ambipolarity the ion flux (for an ion charge Z=1) must balance the electron flux which is influenced by the sheath potential drop V_{sf}. The electron distribution remains Maxwellian in the retarding electric field. Thus, the electron flux to the target reads

$$\Gamma^e_{target} = n_{se}\bar{c_s} = \frac{1}{4}n_{se}\, exp(\frac{eV_{sf}}{kT_e})\sqrt{\frac{8kT_e}{\pi m_e}} \tag{2.18}$$

Equating previous two equations yields

$$\frac{eV_{sf}}{kT_e} = 0.5\, ln(2\pi\frac{m_e}{m_i})(1 + \frac{T_i}{T_e}) \tag{2.19}$$

Typical values for the ratio given above are about 3. To quantify the total potential drop between stagnation plane and target surface one has to add the pre-sheath potential drop [13]

$$V(z) = -\frac{kT_e}{e}\, ln(1 + M_{\|}(z)^2) \tag{2.20}$$

For $M_{\|} = 1$, the total pre-sheath drop is given by $V \approx -0.69kT_e/e$. Emission of electrons from the surface reduces the electrostatic potential. In some cases it can even lead to a breakdown of the sheath. The most important effect is the emission of secondary electrons, but also reflected electrons, photon induced emission and thermal emission play a role. In particular, above certain temperatures thermal emission can dominate and is considered to be one reason for the formation of so called hot spots [21].

2.3.7 Potential drop in the sheath for electrically biased surface

Consider a symmetrical situation, with floating surfaces at each end, and, $V_{sf} = -3kT_e/e$. Next suppose that an external bias is applied to the two end surfaces such that the right end is biased to $-kT_e/e$, relative to the left end surface, Fig. 2.7. Let the voltage drop across the right, and left, sheaths be V_r, and V_l respectively. Both the pre-sheath voltage

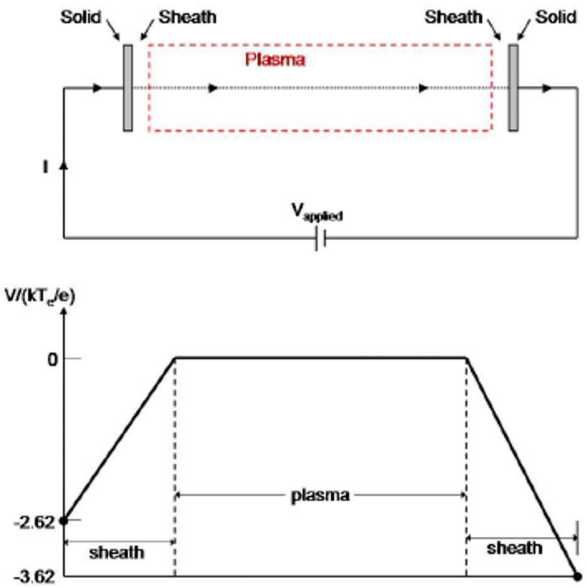

Figure 2.7: *An external power supply applies a potential difference between the two electrically conducting end walls of a 1D plasma/sheath system, drawing a current (top). The potential profile for the case of biasing the right end of the system by* $-kT_e/e$. *Here the plasma potential has been taken as a reference, and it has been assumed that* $V_{sf} = -3kT_e/e$. *The pre-sheath potential drops are not shown here for simplicity (bottom).*

drop would remain at $\sim -0.7kT_e/e$ as before (for simplicity these pre-sheaths are not shown in Fig. 2.7). The electron flux density reaching the right surface will now be

$$\Gamma^e_{rw} = \frac{1}{4} n_{se} \bar{c_e} e^{eV_r/kT_e} \tag{2.21}$$

while

$$\Gamma^i_{rw} = n_{se} c_s = \frac{1}{4} n_{se} \bar{c_s} e^{eV_{sf}/kT_e} \tag{2.22}$$

the same as for $V_{applied} = 0$. Also $n_{se} = \frac{1}{2} n_0$ (isothermal case) as for $V_{applied} = 0$. At the left surface

$$\Gamma^e_{lw} = \frac{1}{4} n_{se} \bar{c_e} e^{eV_l/kT_e} \tag{2.23}$$

and

$$\Gamma^i_{lw} = n_{se} c_s = \frac{1}{4} n_{se} \bar{c_s} e^{eV_{sf}/kT_e} \tag{2.24}$$

by conservation of charge we must have $\Gamma^e_{rw} + \Gamma^e_{lw} = 2 n_{se} c_s$, as well as $V_r - V_l = V_{applied}$. Combining all equations:

$$\frac{eV_l}{kT_e} = ln \left[\frac{2e^{eV_{sf}/kT_e}}{1 + e^{eV_{applied}/kT_e}} \right] \tag{2.25}$$

Finally, we have electron-repelling surface on right, where virtually all of $V_{applied}$ is taken up, while on the left electron-attracting surface saturates - this gives rise the *ion*

saturation current: [3]

$$j_{sat}^{i} \equiv e n_{se} c_s \sim \frac{1}{2} e n_0 c_s \tag{2.26}$$

[3]Some simulations had shown that the coefficient 1/2 should be replaced by ~ 0.35 [22]

Chapter 3

Probes

3.1 Introduction

Probes are active diagnostics in direct contact with the plasma. Therefore, they can only be applied at very plasma edge where the plasma flux does not lead to excessive heating of the probe. The most well known is the *Langmuir probe*. Langmuir probes (LP) provide reliable electron temperature and density diagnostics in relatively cool, low-density plasmas. The probe itself is a small metal electrode - cylindrical, spherical or in the shape of a disk - inserted into the plasma [23]. The sheath that envelops the probe shields the plasma from the probe potential. The essence of the Langmuir probe technique is to monitor the current to the probe as the probe voltage changes. The ideal I-V characteristic of such a single probe is shown in Figure 3.1. If we assume that the current drawn by the probe from the plasma is positive, when the probe bias V is very negative with respect to the plasma potential, V_p, the electric field around the probe will prevent all but the most energetic electrons from reaching the probe, effectively reducing the electron current to zero. The current collected by the probe will then be entirely due to positive ions, since these encounter only an attracting field. This current is called the 'ion-saturation current' I_{is}. As the probe bias is increased, the number of electrons which is able to overcome the repulsive electric field and so contribute a negative current increases exponentially. Eventually the electron current collected is equal to -I_{is}, so that the total current is zero. At this point the floating potential V_f is reached. Further increase of the probe bias to V_p allows the electron current to totally dominate the ion current. At V_p, electrons are unrestricted from being collected by the probe. Any further increase in bias will simply add energy to the electrons, not the current drawn. Hence the term 'electron-saturation current' I_{es}. Note that this is the ideal I-V characteristics, ignoring the 'disturbing' processes such as bombardment of the probe by high energy

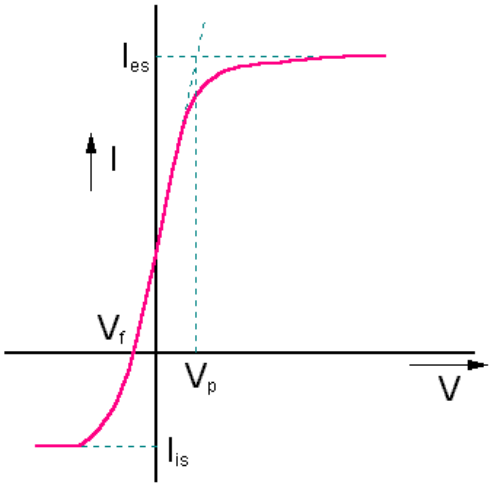

Figure 3.1: *I-V characteristic of an idealized Langmuir probe.*

electrons, emission of secondary electrons from the probe, and the probe etching away.

3.2 Mach probe theory

Mach probe theory, either fluid [22] or kinetic [24], provides a simple relation between the ratio of ion currents and the parallel flow velocity. The basic idea behind a Mach probe is that if the plasma is flowing, then the parallel ion current density measured on each side of the negatively biased probe will be different. The current measured on the upstream side will be larger than that on the downstream side. A strong assumption of the theory is that the electron parallel velocity distribution is Maxwellian.

3.2.1 1D Fluid model

The most convenient approximation used in 1-dimensional models are that the ion density n_i, velocity v_i and plasma potential ϕ at any parallel position x can be regarded as given by single function of x. Under such a condition, we suppose that variables represent a mean value over the perpendicular extent of the collection region. The radius of the collection region is taken to be equal to the probe radius. The cross-field diffusion of ions into the collection region may be represented by a source S in the ion equations which determine the parallel extent of the collection region.

The probe theory is very similar to theory of scrape-off layer (see section 2.3.1). From the SOL model we know that the connection length is fixed by magnetic geometry, and the SOL width is determined by the radial distance that ions can diffuse during their short time-of-flight along field line to the limiter. On the contrary, the plasma is considered to

be infinite and uniform in probe theory. The width of the collection region is then given by the probe dimensions perpendicular to the field. The collection length is the parallel distance that an ion will travel in the time it takes to diffuse across the width of the collection region. The collection region is equivalent to the SOL. The same equations can be applied, only the constraints on the model are different. The SOL width is determined by the connection length whereas the probe collection length is determined by the probe width. In both cases equilibrium solution is determined by the diffusion coefficient.

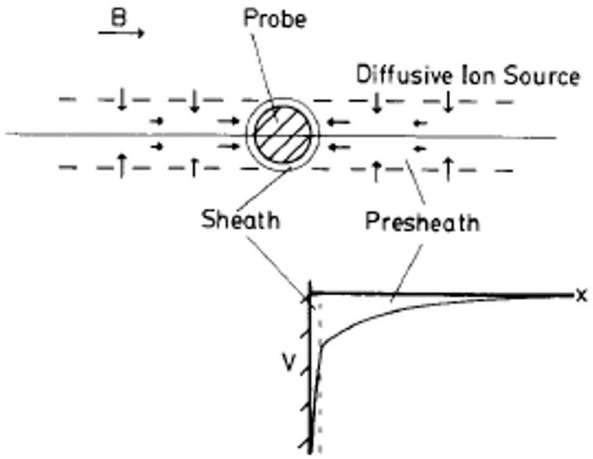

Figure 3.2: *Schematic illustration of hte geometry of ion collection in a strong magnetic field.*

The model presented here was proposed by Hutchinson more than 20 years ago [22]. The model is 1-dimensional and provides a simple relation between the ratio of ion currents collected by the two sides of the Mach probe and the parallel flow velocity. The presheath is modeled as a one-dimensional, two-fluid plasma, which is quasineutral (see Fig. 3.2). Under these conditions, we can replace Poisson's equation by the quasineutrality equation $Zn_i = n_e$ (Z denotes the ion charge). A case in which the majority of electrons are reflected because the probe is sufficiently negative is considered. This allows to use for the electron density a Boltzmann equation

$$n_e = Zn_\infty \, exp(e\phi/T_e) \tag{3.1}$$

Subscript ∞ here denotes quantities in the outer plasma, far away from the collection region, where the potential is taken $\phi = \phi_\infty$ to be zero. The electron temperature T_e is expressed in eV. In the following we consider that the diffusive exchange of ions between the collection region and the outer plasma is given with the frequency Ω. That is, the rate of loss of particles per unit length is $\Omega n_i(x)$ and the rate of gain is Ωn_∞. We can approximate Ω by $D_\perp/a^2$, the diffusive inverse time constant of the collection region for perpendicular diffusion coefficient $D_\perp$.

The steady-state, velocity distribution function $f(\mathbf{x}, \mathbf{v})$ of particles of mass m and charge species α is given by the Vlasov equation

$$\mathbf{v} \cdot \frac{\partial f_\alpha}{\partial \mathbf{x}} + \frac{Q_\alpha}{m_\alpha}(\mathbf{E} + \mathbf{v} \times \mathbf{B})\frac{\partial f_\alpha}{\partial \mathbf{v}} \; = \; \Omega(f_\infty - f_\alpha) \tag{3.2}$$

To obtain the one-dimensional continuity equation we have to multiply equation (3.2) by $d\mathbf{v}$ and integrate

$$\frac{d}{dx}(n_i v_i) \; = \; \Omega(n_\infty - n_i) \tag{3.3}$$

The exchange of momentum between the collection region and the outer plasma is caused by the particles leaving with characteristic momentum $m_i v_i$ and entering with $m_i v_\infty$. Therefore, the momentum equation is

$$n_i m_i v_i \frac{dv_i}{dx} + m_i v_i \Omega(n_\infty - n_i) \; = \; n_i Z e E - \frac{dp_i}{dx} + m_i \Omega(n_\infty v_\infty - n_i v_i) \tag{3.4}$$

where Ze and p_i are the ion charge and pressure, respectively, and $E = -d\phi/dx$ is the electric field. The pressure p_i arises from magnetic equilibria equation $\nabla p = \mathbf{j} \times \mathbf{B}$ (where $\mathbf{j}$ is defined as $\mathbf{j} = \sum Q_\alpha n_\alpha \mathbf{v}_\alpha$). By substituting for $d\phi/dx$ from Eq.3.1 we obtain

$$n_i v_i \frac{dv_i}{dx} \; = \; -c^2 \, \frac{dn_i}{dx} + \Omega n_\infty (v_\infty - v_i) \tag{3.5}$$

To simplify the equation fur further purposes, it has been necessary to ignore a term dT_i/dx arising from dp_i/dx ($p = nkT$) to provide closure of the set of equations. The sound speed c_s corresponding to this approximation is given by

$$c_s^2 \; \equiv \; (ZT_e + T_i)/m_i \tag{3.6}$$

Equation (3.3) and (3.5) are now the plasma pre-sheath equations which need to be solved. After necessary derivations and calculations we obtain the final formula in form

$$\frac{dn}{dM} \; = \; n \cdot \frac{(1-n)M - (M_\infty - M)}{(M_\infty - M)M - (1-n)} \tag{3.7}$$

Applying boundary conditions appropriate to the unperturbed plasma density and flow speed far from the probe, equation (3.11) is integrated numerically from infinity to the probe surface where the Mach number attains the value M = 1, as given by the Bohm criterion. The desired result, namely the ratio of the density on both sides of the Mach probe, was calculated by Hutchinson for flow speeds varying from M_∞ from 0 to 1.

3.3 Probe arrangement

Tore Supra is equipped with two reciprocating probes drives. Both are located in top ports separated by 120° toroidally. They make vertical strokes along the cord R = 2.53

m. The maximum stroke length is $\Delta Z = 0.46$ m below their rest position at $Z = 0.935$ m. By the extensive use of feedback loops and the integration of multiple diagnostic measurements, the reliability of the system has attained a level that allows the probes to be used routinely even in high power, long duration discharges (Figure 3.3). In contrast

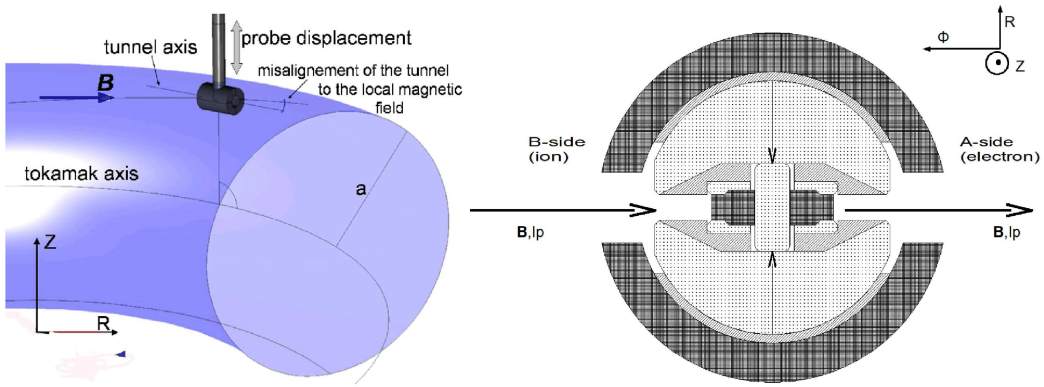

Figure 3.3: *Schematic view of the probe arrangement. On the right is a schematic top view of the tunnel probe.*

to conventional probes that collect charges simultaneously from both directions along the magnetic field lines, Mach probes have directional sensitivity. In their simplest form, Mach probes consist of two Langmuir probes mounted back-to-back on either side of an insulator so as to monitor separately the charged particle fluxes that approach the probe along field lines. In such a arrangement, we can measure the SOL parameters on both sides of the probe (Fig. 3.3 right panel).

The parallel ion current density is calculated by dividing the ion saturation current by the geometrical projection A_{GEO} of the probe along the magnetic field lines [25]:

$$J_{\parallel,i} = \frac{I_{sat,i}}{A_{GEO}} \tag{3.8}$$

The quantities $J_{\parallel,i}, T_e$ and V_f are measured by each pin, then the values on both side of the probe are used to calculate the density and Mach number. The electron density is calculated taking account of the ion flow [24]:

$$n_e = \frac{\sqrt{J^A_{sat,i} J^B_{sat,i}}}{0.35 e c_s} \tag{3.9}$$

where ion sound speed c_s is defined as

$$c_s = \frac{\sqrt{e(T_e + T_i)}}{m_i} \tag{3.10}$$

The T_e and T_i are the electron and ion temperature, respectively. An average value of temperature on sides A and B is used. The parallel Mach number can be derived from the Hutchinson model [24] according to the following formula:

$$M_{||} = 0.4\, ln \left(\frac{J^A_{sat,i}}{J^B_{sat,i}} \right) \tag{3.11}$$

The data that we will present in this work was measured during two different experimental campaigns, in which different types of Langmuir probe pins were used. The relevant technical details of each probe will be summarized in the next sections.

3.4 Tunnel probe

The tunnel probe is a kind of electrostatic probe for use in the scrape-off layer [26]. It provides simultaneous measurements of electron temperature and parallel ion current density with arbitrarily high frequency at the same point in space. The tunnel probe used in these experiments consists of a hollow stainless steel tunnel 3 mm in diameter and 5 mm deep that is closed at one end by en electrically isolated graphite back plate as is shown on Fig 3.4. The conductors are mounted in an insulating boron nitride head and biased

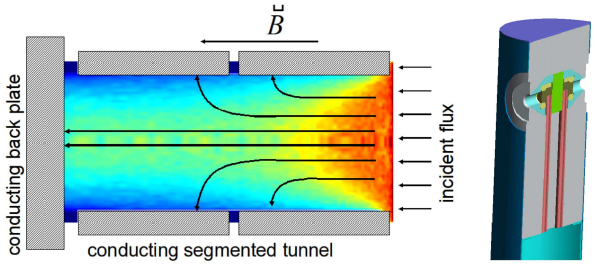

Figure 3.4: *Schematic view of tunnel probe. The current collected by each of the three conductors is monitored separately. The ion guiding center trajectories are shown by black arrows.*

negatively with respect to the tokamak chamber to collect ions and repel electrons. The tunnel axis is parallel to the magnetic field. Plasma flows into the open orifice and the ion flux is distributed between the tunnel and the back plate [25]. The self-consistent interaction between the charge distribution and the electric field inside the tunnel gives rise to two concentric layers of strong radial electric field having different characteristic radial decay length. The first is the positively charged electrostatic Debye sheath that lies adjacent to the tunnel surface and shields the plasma column from the most of the applied probe potential. Its width scales as the square root of the ratio of electron temperature T_e to local electron density n_e. The second layer is the quasineutral magnetic sheath that

scales as the square root of T_e. This magnetic sheath owes its existence to the radial polarization drift of ions. The magnetic sheath is broader than the Debye sheath. The structure of the electric field layers determines the current path inside the tunnel. Ion that enter the strong electric field gradients in either of these two regions are demagnetized and attracted to the tunnel surface. Electrons remain strongly magnetized under all circumstances [27].

The main advantage of tunnel probe is in its concave shape. The concave tunnel probe yields more accurate measurements of T_e and $J_{\parallel,i}$ than conventional convex probes due to the fact that its sheath electric field is entirely contained inside the probe and does not expand into the plasma to perturb the incoming ion orbits. In order to correctly measure the ion current density, the effective collecting area of the probe must be known precisely. For example, the effective area of a small cylindrical pin is larger than its geometrical projection along the field lines due to expansion of the magnetiezed sheath around the probe. This expanding electric field increases the effective collecting area, i.e. ions whose orbits would not intersect the probe in the absence of electric fields are deflected towards the probe and collected. Therefore, the ion current does not saturate for a convex probe, whereas it saturates perfectly for the tunnel probe. Since the sheath electric field depends strongly on density and temperature, it is possible that the effective collecting area can differ on each side of the probe, leading to a falsely deduced Mach number. These problems are eliminated for tunnel probe case, because the sheath is located inside the tunnel. The sheath in this case does not perturb the incoming ion orbits, and the effective collecting area of probe is almost exactly equal to its geometric projection along the field lines, i.e. the effective collecting area is given by the cross section of the orifice $A_{GEO} = \pi r_{orifice}$. [28].

3.5 Sample probe

The sample probe consists of two stainless steel trays that each house five samples whose dimensions are 9 mm x 9 mm x 2 mm. A hole of 0.5 mm diameter is drilled into each sample to accommodate a thermocouple (Fig. 3.5. Five of the samples receive flux from the 'A-side' (electron or downstream side) of the holder, and five from the 'B-side' (ion or upstream side). The samples are numbered '1' to '5' from the deepest position. Nevertheless, for the purposes of this work the most important part of the probe is at the tip of the sample holder where are located two directionally-sensitive Langmuir probes (mounted in Mach probe arrangement) which provide measurements of the ion flux and electron temperature profiles. In contrast to the tunnel probe, the pins at the tip of the sample holder have a convex shape and can be therefore affected by the sheath expansion

effect. For the pins of the sample probe, we take the exposed cross section $A_{GEO} = 24$ mm^2 (6 mm diameter cylinder sticking out 4 mm into the plasma).

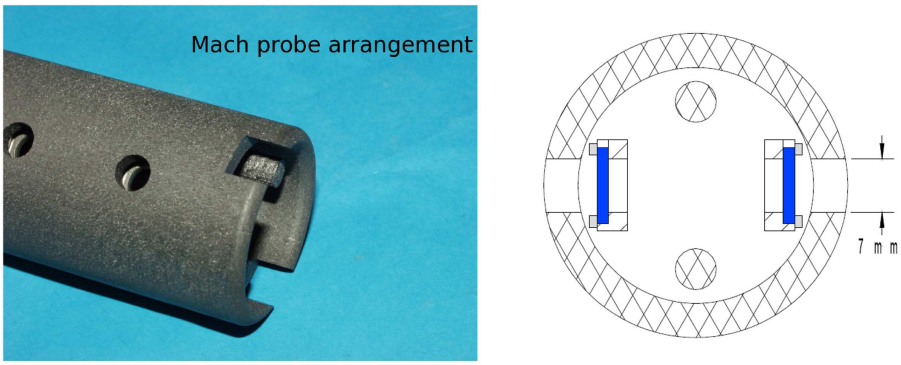

Figure 3.5: *Schematic view of sample probe used on Tore Supra.*

3.6 Example of probe measurements

Radial profiles of basic scrape-off layer parameters of the Tore Supra tokamak measured by a tunnel probe are shown of Fig. 3.6. On the top left panel are shown profiles of ion saturation current on both sides of the probe. It can be seen that current flowing to the B-side of the probe is larger than on the other side. This, according to definition of Mach number (Equation 3.11) means a large flow in the SOL towards to B-side of the probe (bottom right panel) but the flow goes quickly to zero near the LCFS. We believe that this is the transition layer between the SOL where there is large flow to the wall, and the confined plasma where the flow may be different. To protect the probe from destruction by hot plasma, the probe does not go deeply enough to determine whether the core flow is stagnant or of opposite sign to the SOL flow at this particular poloidal angle. The j_{sat} profile on A-side is characterized by a sharp decrease within a small region close to LCFS. On the bottom left panel are then plotted profiles of electron temperature. We can see that even if the probe is small (with respect to the size of vessel) and hence can be assumed that we measure temperature is at a single point in space the profiles on each side of the probe are different. Unfortunately, we do not have model for that, but it probably indicates that the electron distribution is not thermalized. To calculate the ion sound speed, which is needed to calculate the density, we arbitrarily take the average of the two electron temperatures.

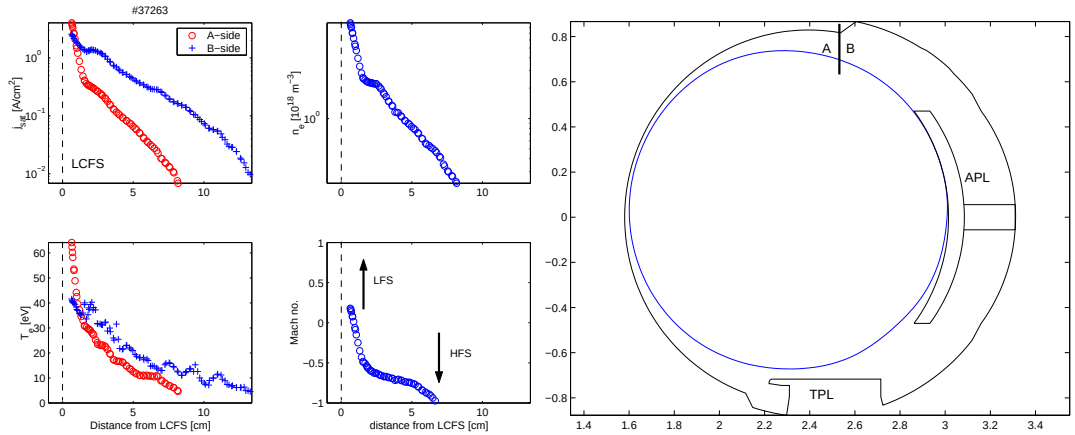

Figure 3.6: *Radial profiles of a basic scrape-off layer parameters of the Tore Supra tokamak.*

Chapter 4

Magnetic field mapping

4.1 Plasma position and shape

The plasma position and shape is on Tore Supra calculated from a set of magnetic flux loops measuring the radial and the poloidal magnetic field and by toroidal flux loops (TFL). All the local field measurements and vertical flux values are corrected in real time for the field created by the current flowing in the TPL structure.

On TS, the plasma position control is achieved by nine, non-equally spaced, poloidal coils. Taking into account the location of these coils, the number and the location of the field sensors in the vacuum vessel has been defined in order to get enough information to be able to act on one positioning coil. The RF coils and PF coils coils are located on a circle in a poloidal plane and installed every 6.5° (Fig. 4.1). Due to a lack of space under the toroidal pumped limiter (TPL), no sensors are mounted at the bottom of the vacuum vessel below an angle of 26.7°. Two types of poloidal arrays have been designed: one consists of 25 PFC and 26 RFC coils, the other consists of 26 PFC and 25 RFC with the PF coils and the RF coils having swapped positions. Three standard arrays are installed at the toroidal locations $\phi = 10°$, 130°, 250° and the three complementary arrays are installed at $\phi = 70°$, 190°, 310°. Therefore, each array has a built-in redundancy of three. Combining the data from an array and its complementary array, 51 radial field measurements and 51 poloidal field measurements are used to define the plasma shape and position. In the previous TS configuration, these quantities were measured by 17 pick-up coils separated by 22° and 17 saddle loops. In order to complete these data, six TFL are mounted at poloidal locations $\theta = 35°$, 57°, 143°, 217°, 303° and 325°. Each loop has a built-in redundancy of two.

This magnetic arrangement provides very good measurement of plasma position and shape only directly under toroidal field coils. But for our purposes, with respect to the probe

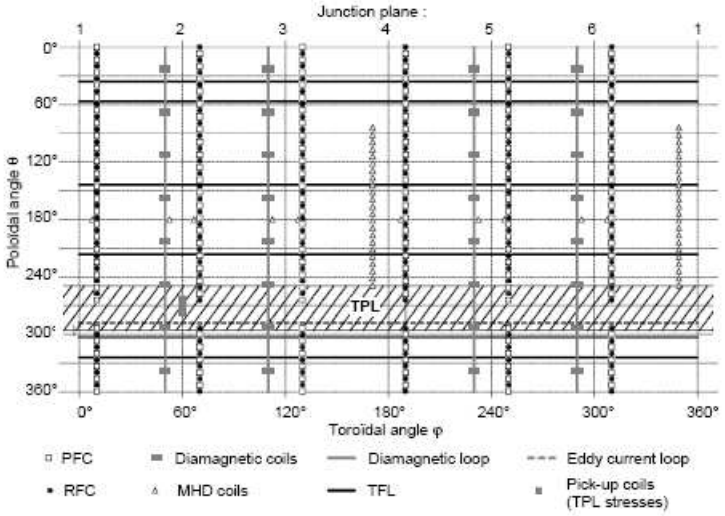

Figure 4.1: *Measurement of plasma position.*

location (160° toroidally), we need to know the magnetic field between TF coils. The toroidal magnetic field in the SOL cannot be described as axisymmetric because it is strongly modulated by the spacing of the 18 superconducting toroidal field coils which are placed every 20° toroidally starting at $\phi = 10°$ with respect to PJ1. The default way in which is on Tore Supra calculated the poloidal magnetic field is schematically shown on Fig. 4.2. To calculate the poloidal magnetic field at a given point between TF coils (Fig.

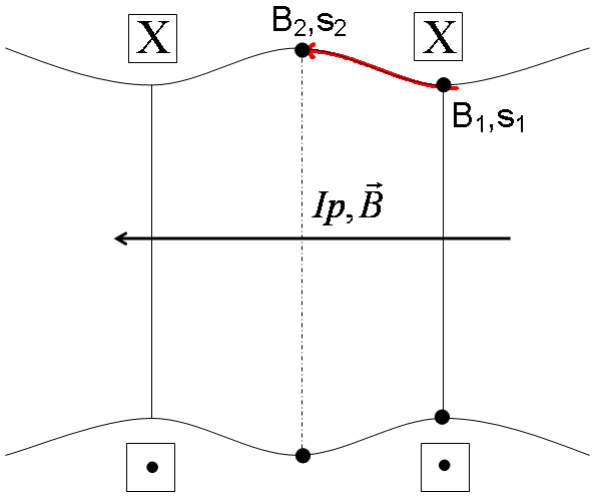

Figure 4.2: *Evaluation of magnetic field between coils by default GRHO signal.*

4.2 point 2) one has to follow a field line from this point of interest to the poloidal plane under TF coil (point 1) and suppose that the poloidal magnetic flux does not change along field line. Unfortunately, some experiments have shown that this approach of magnetic field mapping is not correct.

1) Hot spots location

One of the first problems, which have shown that approach mentioned above is not correct, is concerned with hot spots location of suprathermal electrons [29, 30]. The interaction of the LH suprathermal electrons with the surface of the toroidal limiter, as recorded by the tangential CCD camera #1 in Q4B is shown on Fig. 4.3 According to magnetic field

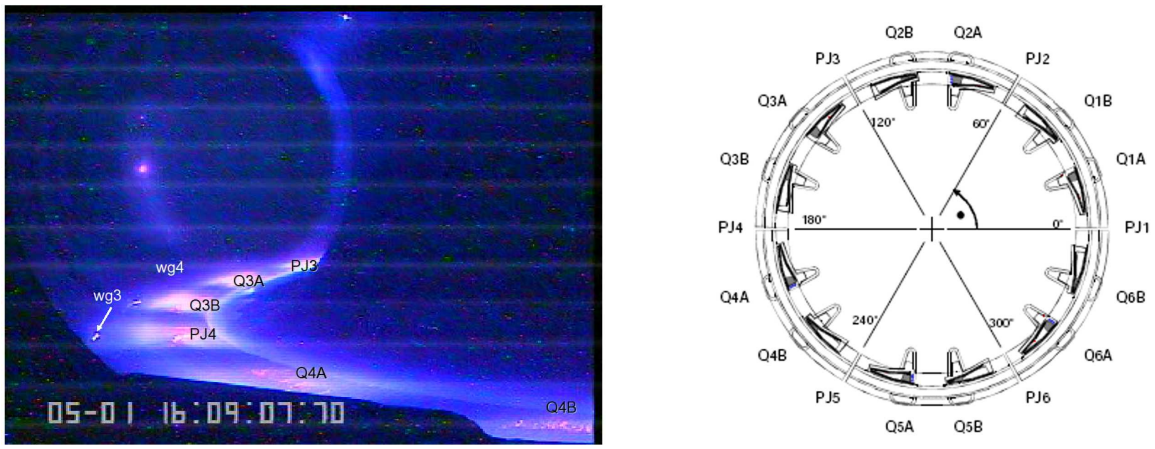

Figure 4.3: *The interaction of the LH suprathermal electrons with the surface of the toroidal limiter. Wg3 and wg4 are the hot spots due to electron acceleration in front of wave guide rows 3 and 4 of the LH2 grill. PJ3, Q3A etc. refer to toroidal positions defined on the right.*

line tracing, the strike point is observed about 20° further away from magnetic prediction. When the measured edge safety factor is between 6.3< q_a <6.5, the hot spot jumps from PJ4 to Q4A and leaves the field of view. One can clearly distinguish the sudden displacement of the strong interaction zone from Q3B to Q4A (i.e. positive toroidal direction) as q is scanned in a continuous way, because of toroidal field ripple. The dark zones on the figure are referred as "private flux" zones and are inaccessible to field lines coming from the SOL. According to magnetics, this event occurs at a lower value of $q_a = 5.95$ (6 to 9% lower). Similarly, to make the magnetics reproduce the jump from Q3B to PJ4, we need to lower q_a by 9 to 13%. To make both jumps agree simultaneously, we have to reduce q_a by 9%. But measurements of q_a are expected to be much more reliable.

2) Ampere's law

Ampere's law relates the integral of the magnetic field strength round a closed loop to the total current enclosed by the loop:

$$I_p = \frac{1}{\mu_0} \oint \vec{B} \cdot d\vec{s} \tag{4.1}$$

The flux conservation theorem which arises from MHD theory postulates that magnetic flux through any surface element remains constant. Closely related is that the flux through

the surface defined by any closed curve within the fluid is also conserved. The result gives rise to the concept of the magnetic flux tube. Let us find a group of field lines which serve as the boundary for a finite volume. Define a closed curve which is the boundary for a small but finite surface (s_1) through which flows non-zero magnetic flux. Follow each field line an arbitrary distance away from the original curve, and define another curve which intersects the same field lines (s_2). This is a "magnetic flux tube".

The approach used by GRHO signal [1] is indeed consistent with a flux conservation theorem, but the problem is in the current which flows into flux tube. If we apply equation 4.1 and calculate the current flowing through the areas enclosed by length s_1 and s_2 we do not get the same result 4.4 leading to discrepancy of about $\sim 2.5\%$ in total current.

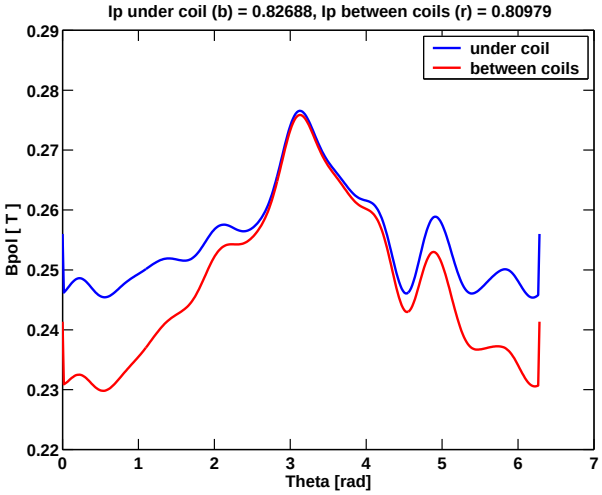

Figure 4.4: *The poloidal magnetic field under the coil and between the coils.*

$$\left.\begin{aligned} I_p(UC) &= 0.83MA \\ I_p(BC) &= 0.81MA \end{aligned}\right\} \qquad \oint B_{\theta 1} \cdot ds_1 \neq \oint B_{\theta 2} \cdot ds_2 \tag{4.2}$$

The correction for this problem is introduced in next section.

[1] GRHO signal serves by default On Tore Supra to obtain a position of LCFS. Its output is a 2-D matrix of R and Z coordinates positions.

4.2 Magnetic field line tracing

As was mentioned above, the toroidal magnetic field in the SOL cannot be described as axisymmetric due to the finite number of toroidal field coils. A 3D map of the vacuum magnetic field $\mathbf{B} = (B_R(R,\phi,Z), B_\phi(R,\phi,Z), B_Z(R,\phi,Z))$ is calculated on a cylindrical grid with good spatial resolution for a current $I_{TF} = 1000$ A. To obtain the TF field for other values of I_{TF}, one simply scales the matrices accordingly.
We assume that the SOL magnetic field is the sum of the vacuum field due to the TF coils and the poloidal field created by the plasma current. The tangential and radial components of the poloidal field are measured by 102 flux loops located on a ring of minor radius 0.92 m centered on major radius 2.42 m. The ring is situated at the same toroidal angle as one of the TF coils. The measured poloidal field is extrapolated radially into the tokamak vessel by third order Taylor expansion to calculate the SOL poloidal field on the cylindrical grid used for the vacuum field. We suppose that the poloidal field that is measured under TF coils is axisymmetric in the SOL, because the plasma current circulates on closed magnetic flux surfaces in the core where TF ripple is minimal (Fig. 4.5). In such a case, the Ampere's law and flux conservation theorem are satisfied [2].

$$\oint B_{\theta 1} \cdot ds_1 = \oint B_{\theta 2} \cdot ds_2 = \oint B_{\theta 3} \cdot ds_3$$

$$\Psi_1 = \Psi_3 \tag{4.3}$$

$$\Psi_1 \neq \Psi_2$$

To calculate a magnetic connection, for example from the probe position to the poloidal plane of the LH antenna, one has to integrate the field line equations. For the small elements of the field line we can write

$$\frac{dl_x}{B_x} = \frac{dl_y}{B_y} = \frac{dl_z}{B_z} \tag{4.4}$$

But for tokamaks is more convenient (with respect to the axisymmetry) to use a cylindrical coordinates in form [31]:

$$\frac{dR}{B_R} = \frac{dZ}{B_Z} = \frac{Rd\phi}{B_\phi} \tag{4.5}$$

By rewriting into differential equations we obtain

$$\frac{dR}{d\phi} = \frac{RB_R}{B_\phi}, \frac{dZ}{d\phi} = \frac{ZB_Z}{B_\phi} \tag{4.6}$$

[2] This is still an assumption. The correct way is somewhere between the method which uses GRHO signal and axisymmetric case

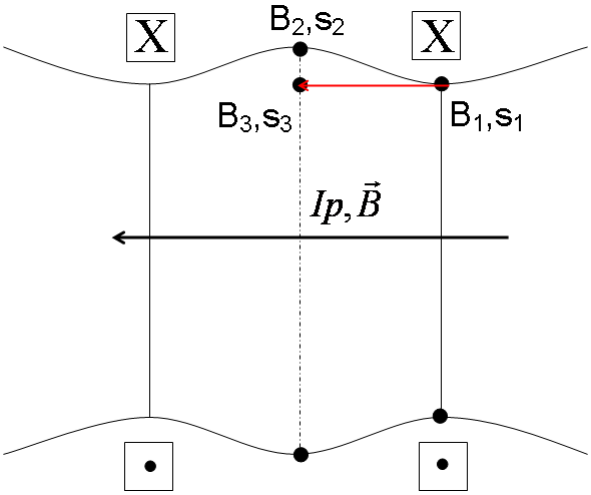

Figure 4.5: *Schematic view of evaluation of magnetic field between coils for axisymmetric case.*

To solve Eqs. 4.6 we are using a second order Runge-Kutta integration scheme, with linear interpolation of the magnetic field from the grid. This is sufficiently accurate for field lines that make less than one full poloidal turn in the SOL. On a Poincaré plot showing intersections of a given field line with poloidal planes situated under TF coils, it can be verified that the field line returns to a surface of constant poloidal flux within ± 0.5 mm radially. Using this new, and indeed simpler method, to calculate the local poloidal field, we are able to reproduce exactly the jumps of LH hot spot positions on the limiter.

4.3 LCFS shift

The knowledge of exact position of last closed flux surface is particularly important from probe's measurement point of view because the hydraulic probe drive is in fact controlled in a real-time feedback loop by the magnetic field diagnostic. The demonstration of LCFS position evaluation by GRHO signal and for axisymmetric case is shown on Fig. 4.6. It can be clearly seen that plasma is bigger on the high field side. The maximal shift is up to 1cm. This implies that profiles measured by the probe are shifted in LCFS direction. The shift can be up to 4 mm for small plasmas.

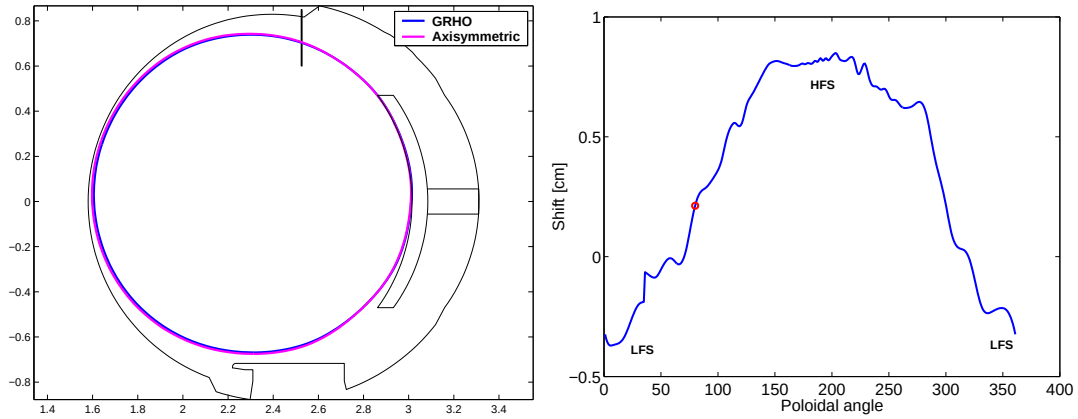

Figure 4.6: *LCFS position obtained from GRHO signal and for axisymmetric poloidal field case. The difference between both methods is on the right. Poloidal probe position is marked by red circle.*

Chapter 5

Results

5.1 ITER startup scenario

The data presented in this chapter are dedicated to experiments that were carried out on Tore Supra to investigate the scrape-off layer conditions in ITER startup scenario. The reference ITER startup scenario for plasma current (I_p) initiation and ramp up is to limit the discharge on two discrete limiters on the low field side (LFS), increasing the minor radius while maintaining q_{95} at the limiter approximately constant at a value $\sim$ 4.8 [32]. In this scenario, the discharge begins on the limiter on the LFS, and the volume monotonically increases in time (see Fig. 5.1) until it is diverted at $t_{ITER} = 55$ s ($I_p =$ 7.5 MA). It shoud be noted that the modulations of the LCFS of the smaller plasmas are not physical, but caused by inaccuracies of the extrapolation of magnetic flux data deep into the chamber.

5.1.1 Tore Supra experiment

Tore Supra is equipped with six modular limiters - one semi-inertially cooled limiter, the antenna protection limiter (APL), and five RF antennas with actively cooled side protection tiles that can be used as limiters. This together with a flexible real-time feedback control system, makes TS the ideal tokamak in which to perform such experiments. The experiments reported here were performed during two experimental campaigns in 2006. Both campaigns are characterized by small plasma minor radius and the plasma current feedback controlled on safety factor $q = 4.6$. During the first campaign, referred here as "ITER startup 1", only one modular limiter (namely the APL located at 140° toroidally, see Fig. 5.2), was used. In "ITER startup 3" was, in addition to the APL, added a second limiter in various radial positions with respect to the APL (the LH2 antenna located opposite to APL at 320° toroidally), and finally, all six limiters were inserted together. The main features of both campaigns are summarized in Table 5.1 below.

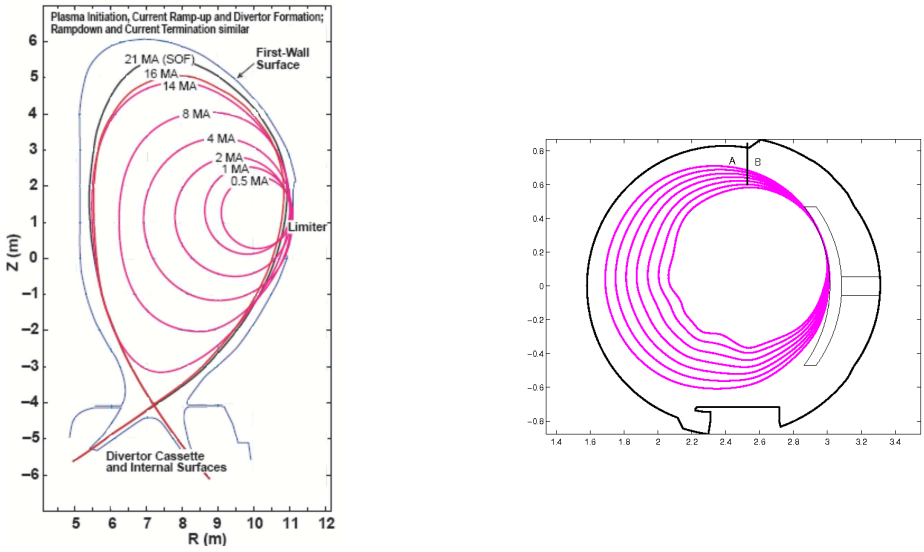

Figure 5.1: *Schematic view of ITER startup scenario. Plasma cross-section expands from the LFS during the current rise, while the edge safety factor is kept roughly constant at a value of about $q \sim 4.8$ (left). The ITER startup scenario configuration in Tore Supra experiment is on the right.*

5.2 ITER1 vs. ITER3

In this section is compared the ITER1 and ITER3 data set. Two situations are distinguished below: In the first case are compared basic SOL parameters profiles of discharges in which only one limiter was used. The shots are characterized by similar core density and plasma minor radius. In the latter case are compared two shots, both from ITER3, but in the first one was used one limiter while in the second 6 limiters were used. Finally, the effects of limiters on edge density, electron temperature and Mach number are discussed.

5.2.1 One modular limiter

On Fig.5.3 are shown profiles of basic SOL parameters such as density, electron temperature, Mach number etc. Two discharges are compared here, one from ITER1 and one from ITER3. Only one limiter (the APL) was used during both shots. The shots are characterized by similar core density $n_e \sim 28.5 \cdot 10^{18} m^{-3}$ and minor radius $a \sim 47cm$. We can see that the shots are very well reproducible. The profiles match almost identically, except electron temperature measurement. The difference in T_e measurements is huge especially on A-side of the probe reaching up to 20 eV. This disagreement is probably caused by the fact that different probes were used in ITER1 and ITER3. A tunnel probe was used in ITER1 whereas in ITER3 the measurements were provided by Mach probe (sample probe). As was mentioned in section 3.4 the difference in T_e measurements might

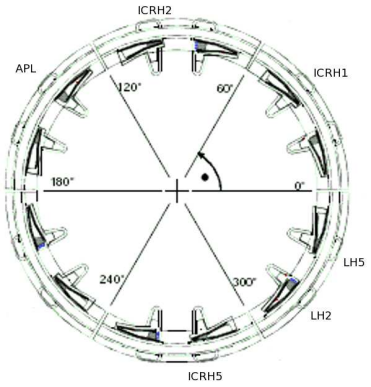

Figure 5.2: *Schematic top view of limiters layout on Tore Supra tokamak.*

	ITER startup 1 (28.6.2006)	**ITER startup 3 (25.10.2006)**
Plasma minor radius	$0.45\text{m} < a < 0.7\text{m}$	$0.45\text{m} < a < 0.65\text{m}$
Plasma current	$0.37\text{MA} < I_p < 1.1\text{MA}$	$0.35\text{MA} < I_p < 0.9\text{MA}$
Toroidal magnetic field	$B_T = 3.86\text{T}$	$B_T = 3.74\text{T}$
Safety factor	$q = 4.6$	$q = 4.6$
Only APL	# 37263-37267, 37275	# 38196, 38205,38206, 38216-38220, 38222
APL + LH2 antenna	————	#38210-38215
All objects	————	#38207-38209

Table 5.1: *Main features of ITER startup campaign.*

be caused by the design of the probes itself. While the sample probe is convex and hence the magnetized sheath expands around the probe which leads to increase of the effective collecting area of the probe, the sheath electric field in tunnel probe is contained inside the tunnel and does not expand outward into the plasma. Moreover, tunnel probe theory assumes perfect saturation of the ion current. Any departure from this dependence causes the fitting routine to interpret the voltage-dependent ion current as electron current, leading to an overestimation of the electron temperature. The sample probe has a rather complex geometry, and the visual inspection of current-voltage characteristics reveals that the ion current does not saturate, whereas that measured by the tunnel probe does.

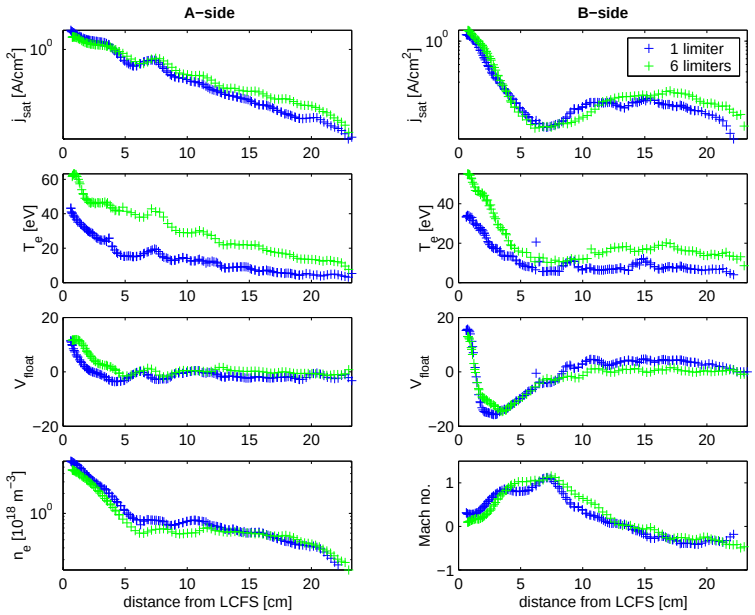

Figure 5.3: *The comparison of basic SOL parameters profiles of ITER1 and ITER3 data set. Only one limiter was used. The shots are very well reproducible. The discrepancy in T_e measurements is probably caused by the sheath expansion effect suffered by the convex pins of the sample probe resulting in a tendency to overestimate the electron temperature.*

If we look on Fig. 5.3 in detail, we can see also big differences in measurements between both sides of the probes. The ion parallel current density (j_{sat}) is decreasing exponentially with the distance from LCFS on side A unlike on B-side, where the decrease is steeper reaching minimal value approximately 7cm from LCFS followed by slow increase. The 'hole' in j_{sat} profile on side B can be interpreted as a effect of discrete limiter shadowing (see section 5.5). This discrepancy in j_{sat} profiles on both sides of the probe has a direct consequence on density (Eq. 3.9) and Mach number (Eq. 3.11) profiles. As a result, the density is characterized by a relatively flat profile on wide region of about ~ 5 cm. On the other hand, the Mach number indicates a huge parallel flow at 'hole' position towards the A-side of the probe. This indicates that field lines coming from the B-side of the probe are connected to the APL, as the magnetic calculations below will show. One can see that floating potential changes a lot too, but it was not the effort of this work to focus on it.

5.2.2 Six modular limiters

The case in which all limiters are pushed inside the vessel is compared with case of one limiter on Fig. 5.4. Both discharges are from ITER3 data set and are characterized by minor radius $a \sim 55.5\,cm$ and core density $n_e \sim 21.5 \cdot 10^{18}\,m^{-3}$. When six limiters are used, only the steep decay region is observed and the flat tail on B-side disappears

completely. With one limiter and small plasma radius we can see bumps on A-side but this phenomena does not occur when all 6 limiters are used. The density profile (bottom left panel) is steeper with all 6 limiters reaching a lower value then in one limiter case as will be confirmed generally in section 5.3.1. The Mach number (bottom right panel) shows that the flow direction is same for both cases but the magnitude is higher with 6 limiters. An interesting situation can be seen. We can see that the current is larger on the on the A-side of the probe, implying flow towards the LFS of the torus.

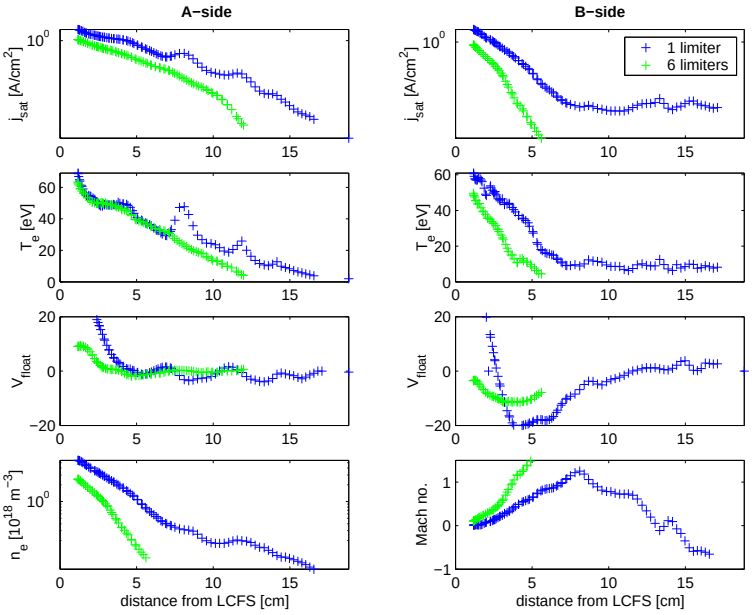

Figure 5.4: *The case in which all limiters are pushed inside (green) the vessel is compared with case of one limiter (blue). Both shots are taken from ITER3 data set. When six limiters are used, the scrape-off layer is very thin ($\lambda_{SOL} \sim 1.5cm$) and only the steep decay region is observed.*

5.3 Effect of limiters

5.3.1 Density

On Fig. 5.5 is plotted edge density in dependence on plasma minor radius with respect to number of used limiters. The density is taken as an average value between 1 - 5 cm from LCFS. Only ITER3 data set is shown here. It can be clearly seen that the density is decreasing with the number of limiters, confirming a general trend indicated by the specific profiles of Fig. 5.4. The density is smaller of about factor of 3 if all limiters are used than in the case with only one limiter.

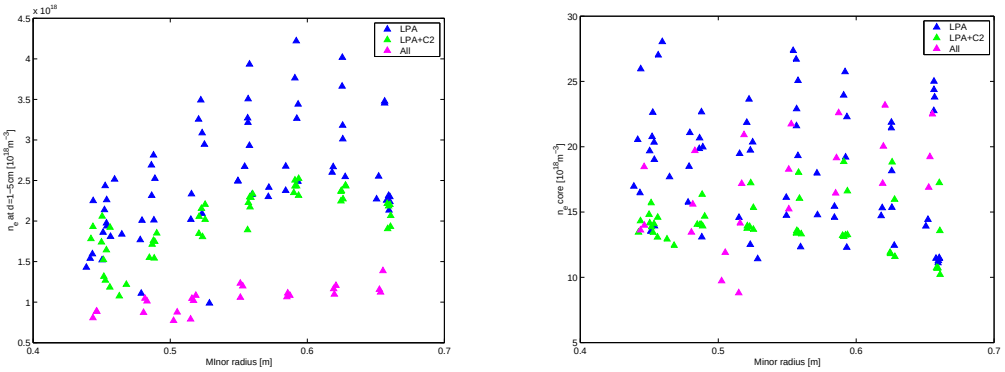

Figure 5.5: *The edge density dependence on number of limiters (left). It can be clearly seen that the density is decreasing with the number of limiters. On the right is plotted similar graph for the core density.*

One notices that for fixed minor radius a there is a large spread in edge density values. The core density is characterized by similar spread for a given minor radius. The connection between the edge density measured by probes and the core density is plotted on Fig. 5.6 - right panel. Despite the scatter of edge density one can see that edge density does generally increase with increasing minor radius. No obvious correlation between the core density and the density measured at plasma edge can be observed due to the scatter (Figure 5.6). Let us focus now only on case with one limiter. If we go deeper in analysis and take points corresponding to a fixed minor radius, in this case 0.58 m $< a <$ 0.71 m, we can clearly see that core and edge density are correlated (Fig. 5.6 - right panel). This is observed only for minor radius greater than 0.58 m. For smaller plasma radii the

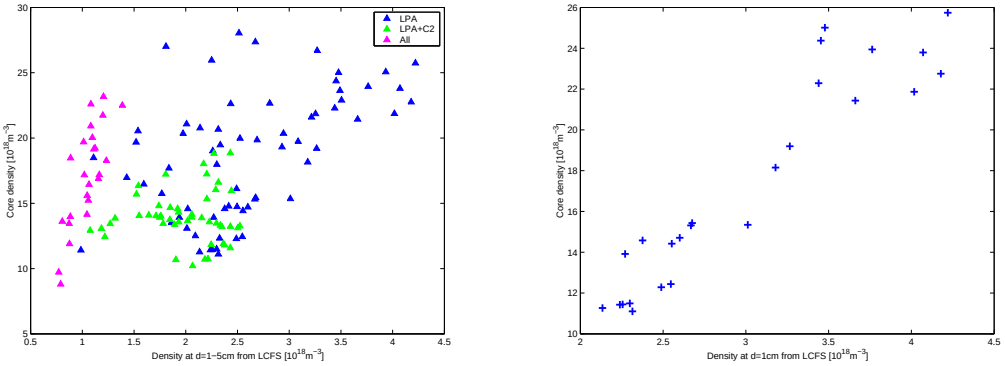

Figure 5.6: *Core density in dependence on edge density with respect to number of limiters. On the right is the same graph but only for one limiter and plasma minor radius 0.58 m $< a <$ 0.71 m.*

link between core and edge density is rather complicated. The relation between core and edge density will be governed by a number of factors, e.g the global particle confinement time (which has never been characterized in these small plasmas) and the details of the

particle recycling in 3D geometry. The complexity of these first results suggests directions for future modelling efforts and complementary experiments.

5.3.2 Temperature

On Fig. 5.7 is plotted edge electron temperature in dependence on plasma minor radius with respect to the number of used limiters. As in previous case, the temperature is taken as an average value between 1 - 5 cm from LCFS. A big difference in measurement is observed on both sides of the probe. Temperature is of about $\sim$ 10eV higher on A-side. This implies non-maxwellian distribution. No obvious dependence on number of limiters can be seen on A-side, unlike on B-side of the probe. A significant drop in temperature can be seen on B-side for all objects in reaching $\sim$ 30 eV which is approximately 2x lower than in comparison with A-side. On the other hand, the measurements using two limiters in opposite ports and with a radial misalignment of 1.0 - 4.0 cm are very similar to that observed with only one limiter.

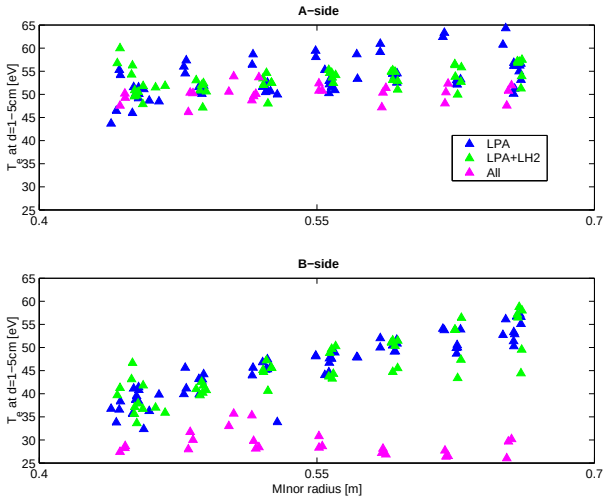

Figure 5.7: *The edge electron temperature dependence on number of limiters. Temperature is of about $\sim$ 10eV higher on A-side. No obvious dependence on number of limiters can be seen on A-side, unlike on B-side of the probe where the temperature drops rapidly for all 6 limiters of factor of 2.*

5.3.3 Mach number

Figure 5.8 shows the variation of Mach number with plasma minor radius. A whole data set is plotted here. Each point on the graph is taken, like in previous cases, as an average between 1 - 5 cm from LCFS. It is nicely seen that case with all limiters has significant effect on plasma behaviour. Let us first consider the case with all limiters. The Mach number in such a case remains constant at a value of about $\sim$ 0.6 and hence the flow is

coming from high field side of the vessel. This result is intuitive. Independently of the magnetic configuration, all field lines originating at the probe position will intersect one of the limiters on the low field side, meaning that the conditions for a simple SOL are satisfied. We therefore expect to see plasma flow directed towards the LFS in all cases. On the contrary, the situation changes dramatically in case with one, or two limiters (limiters are placed in opposite toroidal positions). The Mach number decreases with the minor radius and changes the sign for $a \sim 0.65m$. To understand this observation it will probably be necessary to take account of the detailed 3D connection length map, because some flux tubes will make short connections to LFS limiters, while others have long connection lengths, making several poloidal turns around the chamber (section 5.5). As the plasma minor radius further increases we can see a sharp drop of Mach number resulting in strong negative flow. Big plasmas are limited by inner wall and hence it has an influence of the SOL flow patterns. Analysis of this complicated behaviour might provide information about the poloidal distribution of particle and momentum sources.

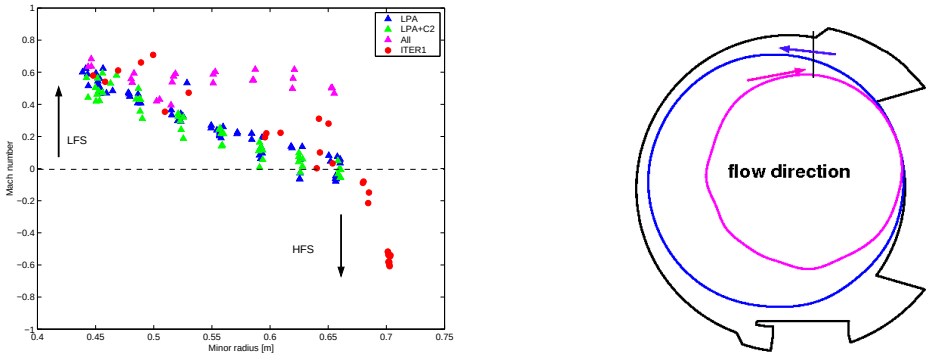

Figure 5.8: *The variation of Mach number with plasma minor radius.*

5.4 Bumps phenomena

The ITER startup scenario has one speciality which is not observed in standard Tore Supra experiment with plasma sitting on bottom toroidal limiter. Some profiles are characterized by local increase of parallel ion current density. This local increase is referred here as a "bump" (see Fig. 5.9). Bumps are real and very well reproducible. Bumps start to be clearly seen on A-side almost for all plasmas smaller than $a < 0.55$ m (except the case with all limiters in which the SOL is very thin). The radial scale of the A-side bumps is of the order of 1 cm.

One of the first idea which can come in mind is that radial position of bumps is somehow connected with plasma size or magnetic configuration. This idea is investigated in detail

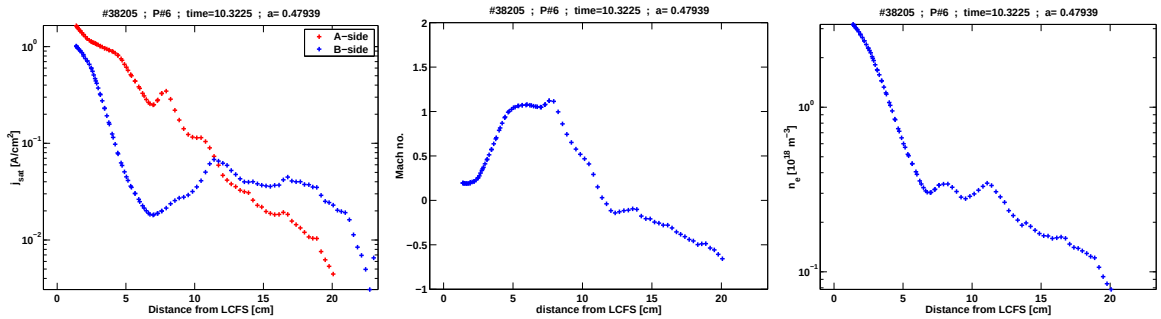

Figure 5.9: *An example view of 'bump' phenomena which occurs only for small plasma radii (left). As a direct consequence we have very high positive parallel flow on bump location and flat density profile on several centimeters.*

in the next section. The bump position does not change during the shot remaining at ~ 7 cm from LCFS independently on plasma minor radius. The increase of parallel ion current density on A-side of the probe is always accompanied by decrease on the opposite side of the probe which position, on the contrary to the A-side bumps, is moving radially and depends on plasma size and magnetic configuration as will be shown in next section. The B-side hole is also significantly wider than the A-side bumps.

Such a measured ion saturation current indicates that plasma conditions are not as usual around bump position. As a result we have very high Mach number on bump location and flat density profile on several centimeters. It can be also seen that the scrape-off layer can be divided into two regions. The first region closely to LCFS is characterized by strong positive parallel flow (from inboards to outboards) and sharp density decrease while in the region far away from LCFS the flow changes direction and density decrease starts to be moderate.

5.5 Connection lengths

As was mentioned in previous section some profiles are characterized by local increase of parallel ion current density (j_{sat}). The bump radial position from LCFS remains constant independently on plasma minor radius. Another idea is to check the connection lengths connected with the probe. To determine if the particle following a field line, which is connected to probe, hits an object inside the vessel we solve a field line equation which is in cylindrical coordinates expressed as

$$\frac{dR}{d\phi} = \frac{RB_R}{B_\phi}, \frac{dZ}{d\phi} = \frac{ZB_Z}{B_\phi} \tag{5.1}$$

As particle is moving along field line a matlab routine checks whether or not the field line intersects any object inside the vessel (or vessel itself). Each object is defined by

several planes which define object's 3D shape. Then a dot product of particle coordinates with each plane is calculated to confirm whether the field line is inside or outside of the object. In total, we distinguished following objects: APL, 5 antennas, toroidal bottom limiter and upper and lower part of the vessel. The principal object which is inserted into the vessel is antenna protection limiter (APL) (see Figure 2.3). The APL consists of a blade which interacts directly with edge plasma and a movable boom which holds the blade. The thickness of the blade is 7.4 cm, the poloidal radius of curvature of APL is 80 cm, the full toroidal width is 34.4 cm and the height of the blade is 110 cm. The boom is a 10 cm diameter cylinder but for simplicity a rectangular shape is used in model.

Figure 5.10 shows connection length for bump case. It can be seen that the 'hole' in the B-side j_{sat} profile is caused by the shadow of APL blade. The connection lengths are very short on width of about $\sim$ 7 cm which is exactly the thickness of the blade (Figure 5.10 right). The flow direction is towards the blade in this layer and due to the short connections lengths of flux tubes the flow is very strong. Further away from LCFS, at $d_{LCFS} = 10cm$, particles do not hit the blade, can escape behind the blade and can even pass below the outboard midplane without hitting any limiter. Hence, very long connection lengths are observed which states that APL is not a good limiter. These measurements show that incomplete poloidal coverage by the limiter can lead to very broad SOL profiles, with complex structures that depend on the specific 3D magnetic topography.

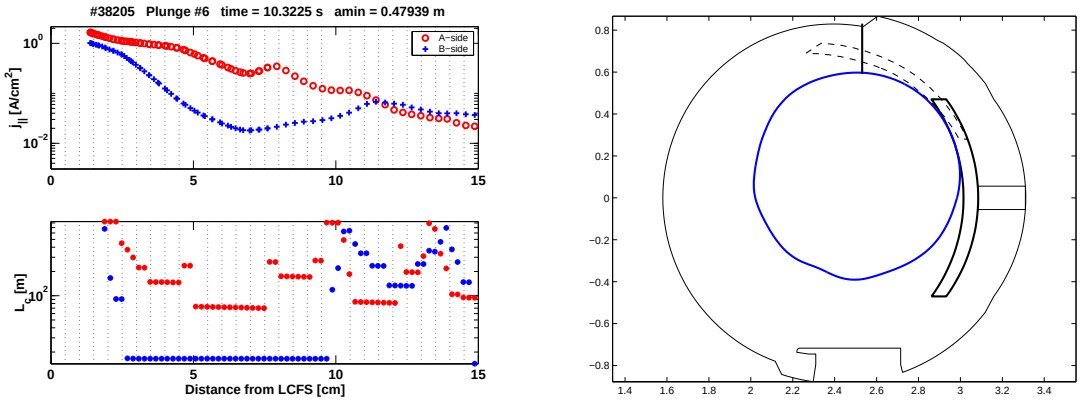

Figure 5.10: *The link between bump phenomena and connection lengths is on the left. No obvious correlation between bump and connection length is observed. On the other hand, the magnetic calculations show that the hole on B-side of j_{sat} profile is caused by limiter shadowing effect which is shown on the right panel. The dashed line represent the APL blade shadow. Connection length on lower left panel which are $L_c > 100m$* corresponds to $N_{pol} > 1$.

Some recent studies about flows in Tore Supra tokamak have shown that the SOL is very thin when the is leaning on the LFS limiters (all 6 limiters case), but very broad when on HFS limiters [33]. One of the results of the studies was that radial transport is either reduced due to the contact with LFS limiters (maybe a modification of turbulence), or that the transport is not modified, but simply that the plasma that gets ejected into the SOL on the LFS is intercepted by one of the 6 limiters before it can flow up to the probe. In addition to that we see the transport seems to be dependent on toroidal position, in particular, whether the field lines are connected to a limiter or not. Let us consider the field line at 10 cm from the LCFS. Then follow it from the probe to the outer midplane. At that point, if we imagine a horizontal radial cord directed towards the LCFS we will not find any object anywhere along that cord. This might mean that plasma is being convected radially from the LCFS to positions very far away, up to the wall. Depending on the pitch of the field lines (which is a function of radius), some of the plasma will intersect limiters, but some will not. Consequently, the presence of a single limiter at the LCFS does not modify the global physics of SOL turbulence, i.e. the blobs still exist, and they still propagate radially.

Unfortunately, there is no link between A-side bumps and long connection lengths as was expected. We can see that there are several regions in which long connection lengths are followed by short ones and vice versa. These measurements show that scrape-off layer is complex and is not axisymmetric, i.e. whether or not the probe is connected to the APL depends on the local pitch angle of the magnetic field lines, which varies rapidly with radius in the SOL. It should be pointed out that connection length is simple approximation. We suppose that particle follows field line strictly and is not affected by collisions, diffusion or any other processes. Hence, only short connection lengths can be taken into account. The fine radial scale of the A-side bumps might be related to the connection lengths, but we cannot get qualitative agreement due to inaccuracies of magnetic reconstruction for small plasma, long connection lengths, and possible the plasma transport phenomena mentioned above. It was calculated recently that radial transport "smears out" fine scale features of the connection mapping that propagate more than one poloidal turn [34].

5.5.1 Connection length mapping

Figure 5.11 then shows connection lengths mapping. The graphs show connections lengths mapped from the probe plane, i.e. starting at 160° toroidally. On the left panel, we can see how complex the scrape-off layer is. A shadow of the APL blade is located on the top of the vessel. This corresponds to particles which hit the blade on first turn around the

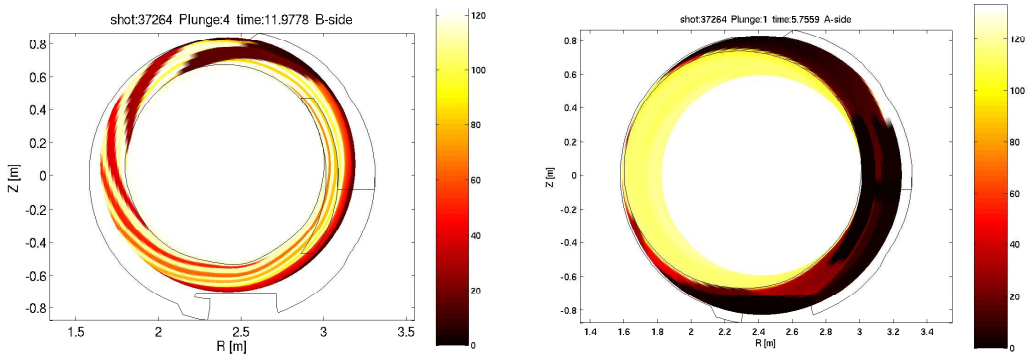

Figure 5.11: *A 2D map of connection lengths in probe plane. A simple SOL is shown of left, simple SOL on right. Yellow colour indicates that no connection was found due to the imposed limits of the field line integral.*

vessel. Then we can see as the blade shadow is moving in counter-clockwise direction as particles hitting the blade on second, third ... turn. It should be pointed out that the direction of integration of the field line equations is taken from the probe towards the low field side. To visualize the connection length map in the other direction, it is sufficient to place the probe at the bottom of the machine. There we see much finer scale radial variations of connection length due to magnetic shear. On the right panel is shown case of simple scrape-off layer which is typical for big plasmas limited by inner wall. A whole APL can be nicely seen on this graph. A similar 3D analysis of ITER startup configuration can be found here [34]. Complicated connection length maps were also found, so we can conclude that the Tore Supra experiments can be useful for providing experimental data to help model ITER startup.

Conclusion

The study of edge plasma physics in tokamaks has developed rapidly in recent years and is now considered as one of the major research areas to be addressed both in present and future machines. Edge probe techniques are necessary experimental contribution to such studies, providing information about the basic plasma parameters.

This thesis is dedicated to experiments that were carried out on Tore Supra tokamak to investigate the scrape-off layer conditions in ITER startup scenario. The reference ITER startup scenario for plasma current initiation and ramp up is to limit the discharge on two discrete limiters on the low field side (LFS), increasing the minor radius while maintaining q_{95} at the limiter approximately constant at a value ~ 4.8. The experiments reported here were performed during two experimental campaigns in 2006. A variable number of limiters were used in these experiments. We focus here mainly on magnetic reconstruction and magnetic field mapping and on preliminary analysis of edge plasma probe measurements.

A significant improvement was achieved in magnetic field calculations, especially in magnetic connections between objects over less than 1 poloidal turn. However, the new calculations show that the discrepancy between ours and standard method for LCFS evaluation (which we showed is not correct in its nature) can be neglected.

It was found out that the number of limiters has huge effect on plasma behaviour. The edge density decreases with number of limiters and reaches the value of about 3 times smaller if all limiters are used than in the case with only one limiter. A clear correlation between core and edge density was found for plasma minor radius greater than 0.58 m.

Similar observations are seen for electron temperature. Temperature is of about ~ 10 eV higher on A-side which shows to a non-maxwellian distribution. No obvious dependence on number of limiters is observed on A-side of the probe, unlike on B-side of the probe where the temperature drops rapidly for all 6 limiters of factor of 2. On the other hand, the measurements using two limiters in opposite ports are very similar to those observed with only one limiter.

Another interesting edge plasma parameter presented here is parallel Mach number. The case with all limiters has significant effect on plasma behaviour. The observations with all 6 limiters differ from those with one or two limiters. The Mach number in such a case remains constant at a value of about ~ 0.6 and hence the flow is towards the A-side of the probe coming from high field side of the vessel. On the contrary, in case with one, or two limiters, the Mach number decreases with the minor radius and changes the sign $a \sim 0.65m$. As the plasma minor radius further increases a sharp drop of Mach number occurs. To understand this observation it will probably be necessary to take account of the detailed 3D studies.

It was found out that plasmas with minor radius smaller than 0.55 m are characterized on A-side of the probe by local increases of parallel ion current density. These bumps are real and very well reproducible. The bump position does not change during the shot remaining at ~ 7 cm from LCFS independently on plasma minor radius. This phenomena is always accompanied by a decrease on the opposite side of the probe.

Magnetic field calculations show, that this 'hole' in j_{sat} profile is caused by the shadow of APL blade. The flow direction is towards the blade and due to the short connections lengths of flux tubes the flow is very strong. Thanks to the finite thickness of the APL blade some particles do not hit the blade, can escape behind the blade and can even pass below the outboard midplane without hitting any limiter. This shows that the plasma can propagate very far radially if it does not intercept a discrete limiter. The existence of regions with very long connection lengths means that APL is not a good limiter and the scrape-off layer is complex and not axisymmetric. Only for big plasma a simple scrape-off layer is observed.

In conclusion should be noted that calculations used for magnetic field line tracing is simple approximation. We suppose that particle follows field line strictly and is not affected by collisions, diffusion or any other processes. Hence, only short connection lengths can be taken into account. We see that number of limiter has significant effect on SOL behaviour. Pushing 6 limiters in confirms that the tail of the SOL profiles is due to transport that is localized on the LFS. If the same kind of transport occurred at other poloidal positions, we would not expect to see such strong changes in the profiles. Some clear trends have been already identified, but not for all them do we have an explanation. Lot of results presented in this work were achieved at the end of stay, are of a preliminary nature and require further investigation both on experimental and theoretical field.

Bibliography

[1] M. für Plasmaphysics, *IPP Summer University for Plasma Physics, Greifswald, Germany*. September 26 - 30, 2005.

[2] J. Wesson, *Tokamaks*. Clarendon Press, Oxford, 3 ed., 2004.

[3] J. D. Lawson, "Proceedings of the physical society b," vol. 70, p. 6, 1957.

[4] P. E. S. C M Braams, *Nuclear Fusion: half a century of magnetic confinement research*. Institute of Physics Publishing, ISBN: 0750307056, 2002.

[5] R. R. Weyrants, "Fusion machines," *Fusion Science and Technology*, vol. 49, no. T2, pp. 36 –42, 2006.

[6] M.-P. I. f. P. project W7X, Greifswald http://www.ipp.mpg.de/ippcms/de/for/projekte/w7x/.

[7] D. A. Hartmann, "Stellarators," *Fusion Science and Technology*, vol. 49, no. T2, pp. 43 – 55, 2006.

[8] T. Supra http://www.cea.fr.

[9] J. Mlynar, *Focus on: JET*. EFD-R(07)01.

[10] W. M. Stacey, *Fusion Plasma Physics*. John Wiley, ISBN 3-527-40586-0, 2005.

[11] F. Wagner *Phys. Rev. Lett.*, vol. 49, no. 1408, 1982.

[12] P. C. Stangeby, *The Plasma Boundary of Magnetic Fusion Devices*. Institute of Physical Publishing Bristol and Philadelphia, 2000.

[13] B. Unterberg *Fusion Science and Technology*, vol. 49, no. T2, pp. 215 –233, 2006.

[14] P. C. Stangeby and G. M. McCracken *Nucl. Fusion*, vol. 30, no. 1225, 1990.

[15] P. C. Stangeby, *The Plasma Boundary of Magnetic Fusion Devices*. Institute of Physical Publishing Bristol and Philadelphia, 2000.

[16] R. J. Goldston and P. H. Rutherford, *Introduction to Plasma Physics*. Bristol: Institute of Physics Publishing, 1997.

[17] F. F. Chen, *Introduction to Plasma Physics and Controlled Fusion*. New York: Plenum Press, 2006.

[18] P. M. Bellan, *Fundamentals of Plasma Physics*. Cambridge University Press, ISBN 0521821169, 2006.

[19] D. Bohm, *The Characteristics of Electrical Discharges in Magnetic Fields*. New York: McGraw-Hill, 1949.

[20] E. R. Harrison and Thompson *Proc. R.Soc. A*, vol. 72, no. 2145, 1995.

[21] V. Philipps *Nucl. Fusion*, vol. 33 (6), no. 953, 1993.

[22] I. H. Hutchinson *Phys. Fluids*, vol. 30, no. 12, 1987.

[23] I. H. Hutchinson, *Principles of Plasma Diagnostics*. Cambridge University Press, 2nd edition,ISBN-10: 0521803896, 2002.

[24] K. S. Chung and I. H. Hutchinson *Phys. Rev. A*, vol. 38, p. 4721, 1988.

[25] J. P. Gunn *Phys. Plasmas*, vol. 8, no. 1040, 2001.

[26] J. P. Gunn *Czech J. Phys.*, vol. 52, no. 1107, 2002.

[27] J. P. Gunn *Czech J. Phys.*, vol. 55, no. 3, pp. 255–263, 2005.

[28] J. P. Gunn, "Aip conference proceedins," vol. 812, pp. 27–34, 2006.

[29] M. Goniche *Nucl. Fusion*, vol. 38, no. 919, 1998.

[30] J. P. Gunn *J Nucl. Mater*, 2009.

[31] P. J. Morrison *Phys. Plasmas*, vol. 7, no. 6, 2000.

[32] "Iter technial basis, plant description document, section 3.7.4.1," tech. rep., 2002.

[33] J. P. Gunn *J Nucl. Mater.*, vol. 290-293, pp. 877–881, 2001.

[34] M. Kobayashi *Nucl. Fusion*, vol. 47, pp. 61–73, 2007.